JESCEE
Journal of Emerging Supply Chain, Clean Energy, and Process Engineering

p-ISSN 2963-8577
e-ISSN 2964-3511

Vol 3. No 2. 2024

JESCEE | Vol. 3 | No. 2 | pp. 69 - 119 | JAKARTA 2024 | ISSN 2963-8577

Faculty of Industrial Technology Universitas Pertamina

Universitas Pertamina

Journal of

Emerging Supply Chain, Clean Energy, and Process Engineering

Vol 3, No 2, 2024

Journal of
Emerging Supply Chain, Clean Energy, and Process Engineering
Vol 3, No 2, 2024

Journal of

Emerging Supply Chain, Clean Energy, and Process Engineering

Vol 3, No 2, 2024

Reviewers

1. Dr. Dr. Eng. Imam Wahyudi Farid, S.T., M.T. (Institut Teknologi Sepuluh Nopember, Indonesia)
2. Dr. Eng. Muhammad Abdillah, S.T., M.T. (Universitas Pertamina, Indonesia)
3. Dr. Eng. Rizal Mahmud, S.Pd., M.T. (Badan Riset dan Inovasi Nasional (BRIN), Indonesia)
4. Dr. Eng. Agus Susanto, S.Pd., M.T. (Politeknik Negeri Madiun, Indonesia)
5. Herlambang Setiadi, Ph.D. (Universitas Telkom, Indonesia)
6. Dr. Soni Prayogi (Universitas Pertamina, Indonesia)
7. Dr. Catia Angli Curie (Universitas Pertamina, Indonesia)
8. Eduardus Budi Nursanto, Ph.D (Universitas Pertamina, Indonesia)

Imprint

JESCEE is published by Faculty of Industrial Technology, Universitas Pertamina, Jakarta Selatan, Indonesia.

Postal Address

JESCEE Secretariat:

Universitas Pertamina

Jl. Teuku Nyak Arief, Simprug, Kebayoran Lama, Jakarta Selatan, 12220

Indonesias

Business hour: Monday to Friday

07:00 to 17:00 GMT+7

e-mail: jescee@universitaspertamina.ac.id

Journal of
Emerging Supply Chain, Clean Energy, and Process Engineering
Vol 3, No 2, 2024

PREFACE

The Journal of Emerging Supply Chain, Clean Energy, and Process Engineering (JESCEE) is published by the Faculty of Industrial Technology at Universitas Pertamina. It fosters communication among researchers, disseminates research findings, cultivates an academic culture, and encourages the development of new ideas in the fields of mechanical, electrical, chemical, and logistics engineering. The journal's Volume 3, Issue No. 2, has attracted significant attention from numerous researchers eager to publish their work.

On behalf of the Editor-in-Chief, I would like to extend my gratitude to everyone who supports this journal, especially the Dean of the Faculty of Industrial Technology for their direct and indirect assistance. I also appreciate the dedicated editors, the reviewers who provide valuable suggestions and constructive feedback on each submitted paper, and the authors who trust JESCEE with publishing their research.

We hope that this publication will continue to grow and present the latest information in the fields of mechanical, electrical, chemical, and logistics engineering. We also welcome collaborations from individuals and organizations that value this journal and wish to contribute to its ongoing development.

Jakarta, December 2024
Editor-in-Chief

Dr. Eng. Muhammad Abdillah

Journal of

Emerging Supply Chain, Clean Energy, and Process Engineering

Vol 3, No 2, 2024

List of Contents

Vol. 03, No. 2, December 2024, pp. 69-78
p-ISSN: 2963-8577
e-ISSN: 2964-3511
DOI: 10.57102/jescee.v3i2.82

QUANTIFYING MEASUREMENT UNCERTAINTY USING WEIGHTED LEAST SQUARES FOR FORCE MEASUREMENT IN BIOMIMETIC ROBOT DEVELOPMENT

Muhammad Farhan[1], Arie Sukma Jaya[1*]
[1]Department of Mechanical Engineering, Faculty of Industrial Technology, Universitas Pertamina

Abstract
Robotics is one area where biomimetics, a field devoted to mimicking natural systems to address difficult human problems, has made great strides. Precise force measurement and analysis are vital to this field because they are necessary to reproduce and comprehend natural phenomena. This study addresses the challenge of accurate force measurement by developing a load cell-based device. It specifically assesses the impact of the taring process on measurement accuracy. The Weighted Least Squares (WLS) method is employed to thoroughly quantify the uncertainty of the device, ensuring reliability. The findings suggest that the single-input taring process contributes to variations in standard deviation, with accuracy peaking near the tared value and decreasing as the mass deviates from it. The linear calibration equation derived from WLS showed minimal variation in estimated mass values, with uncertainties $u_a = 2 \times 10^{-6}$ and $u_b = 8 \times 10^{-4}$. However, the expanded uncertainty increased with the input mass, largely due to the inherent uncertainty of the mass balance. Despite this, the hysteresis of the system was negligible, and its sensitivity of 0.01 N/g made it suitable for detecting small force fluctuations in biomimetic models. The study concludes that while the relative value of the maximum combined uncertainty, U_{Lc} = ±0.2% FSS, exceeds the reference specifications of the load cell, it remains adequate for applications requiring moderate precision. Future research will reduce mass balance uncertainty and consider environmental factors, thereby improving system effectiveness in biomimetic research.

Keywords:
Force measurement; uncertainty; weighted least squares (WLS); biomimetics; robotics

Article History:
Received: August 10th, 2024
Revised: November 29th, 2024
Accepted: December 11th, 2024
Published: December 13rd, 2024

Corresponding Author:
Arie Sukma Jaya
Department of Mechanical Engineering, Universitas Pertamina, Indonesia
Email:
arie.sj@universitaspertamina.ac.id

1. Introduction

Biomimetics has recently emerged as a dynamic field of study that seeks to solve complex human problems by emulating natural models, systems, and elements [1,2,3]. Observing and mimicking natural processes has allowed this multidisciplinary approach to be applied to a variety of domains, including robotics, materials science, and medical devices. The essence of biomimetics is its ability to obtain inspiration from the efficiency and adaptability of biological systems [4,5,6]. However, the successful implementation of these nature-inspired solutions frequently relies on precise measurement and analysis, particularly in the context of forces and interactions, which are critical for understanding and replicating natural phenomena. Precision force measurements are required for more than just data collection; they are critical for validating theoretical models and ensuring experiment reproducibility [7,8,9,10]. As a result, developing tools that can precisely measure these forces is a critical challenge in the advancement of biomimetics.

High precision in force measurement instruments is required due to the inherent uncertainties that can arise during experiments [11,12,13]. These uncertainties can come from a variety of sources, including environmental factors, instrument calibration, and the intrinsic properties of the materials under investigation. Inaccurate force

measurements can cause significant errors in data interpretation, potentially leading to false conclusions about the behavior of the biomimetic systems under investigation. Thus, reducing these uncertainties is critical for achieving reliable and reproducible results. To address these challenges, researchers must improve the sensitivity and accuracy of their measurement tools and thoroughly quantify and account for any uncertainties in their data.

This study aims to develop a force measurement device using a simple yet highly precise load cell. By optimizing its design and calibration, the research seeks to achieve exceptional accuracy in force measurements, making the device ideal for delicate and detailed biomimetic studies. The simplicity of the device is intentionally designed to ensure accessibility and ease of use, without sacrificing measurement accuracy or reliability. While most available load cells are compatible with microcontroller boards via ADC modules that enable taring—a common practice that sets the baseline for measurements—the accuracy of this process has not been thoroughly assessed. This study addresses this gap by quantifying the uncertainty in tared load cell measurement systems. To quantify the uncertainty associated with the developed force measurement device, this study employs the Weighted Least Square (WLS) method [14,15,16]. The WLS method is a statistical approach that accounts for varying levels of uncertainty in different measurements, providing a more accurate estimation of the parameters being studied. By applying WLS, the study aims to identify and minimize the sources of uncertainty in the measurements, thus enhancing the overall reliability of the device. This approach not only improves the precision of the measurements but also provides a robust framework for assessing the quality of the data obtained. The use of WLS is particularly advantageous in biomimetic research, where the forces involved can be extremely small and sensitive to a wide range of factors. The ultimate goal of this research is to develop a reliable force measurement system for biomimetic studies, with a focus on rigorously quantifying its uncertainty. The uncertainty calculated using the WLS method will be compared with the initial load cell specifications to validate the performance of the device. Additionally, the developed setup will be tested in preliminary continuous force measurements of a biomimetic model. The outcomes of this study are expected to significantly advance the field of biomimetics, providing researchers with new tools and methodologies to explore the intricate interactions within natural systems.

2. Method

A. Calibration and uncertainty quantification

The current study utilizes the Weighted Least Square (WLS) method to approximate linear equations and directly calculate the uncertainty of measured parameters. It links the actual mass of the load with the output reading of the measured mass through the linear Equation (1):

$$m_C = b + a\, x_c \tag{1}$$

where m_c is the actual mass of in grams, b is the intercept constant, a is the slope of the calibration curve, and x_c is the output reading of the measured mass in grams. The coefficient vector, C, is calculated using Equation (2) where X represents the average measured values, Y denotes the reference values, and superscript T indicates the transpose of the parameters.

$$(X^T.X).C = X^T.Y \tag{2}$$

$$X = \begin{bmatrix} x_{1,1} & x_{1,2} \\ \vdots & \vdots \\ x_{j,1} & x_{j,2} \end{bmatrix} \tag{3}$$

$$Y = \begin{bmatrix} \frac{m_{c,1}}{w_1} \\ \vdots \\ \frac{m_{c,j}}{w_j} \end{bmatrix} \tag{4}$$

$$w_j = \sigma_{x_i}^2 \tag{5}$$

$$Q = (X^T.X)^{-1} \tag{6}$$

In the Equation (3) X is a j x 2 matrix with elements $x_{j,1} = \frac{1}{w_j}$ and $x_{j,2} = \frac{x_i}{w_j}$, where x_i is the output reading of the measured mass using a bar load cell. The column vector Y in Equation (4) represents the weighted value of the input mass, determined by dividing the actual mass, m_c, by a weighting factor, w_j. The weighting factor, w_j, as defined in Equation (5) is derived from the variance of the output reading x_j. Equation (6) describes the Q matrix, where the diagonal elements represent the variance of the linear equation coefficients a and b, and the off-diagonal elements represent their covariance. Uncertainty is a parameter that indicates the distribution of a measured quantity [17,18,19]. In this study, two types of uncertainty are considered: type A and type B. Type A uncertainty is calculated through repeated direct measurements, while type B uncertainty is based on existing information, such as manufacturing specifications and reference data. The type A uncertainty of forces, based on calibration values, u_L, follows the law of uncertainty propagation in Equation (7):

$$u_L = \left(a^2 u_{mo}^2 + u_b^2 + m_o^2 u_a^2 + 2m_o Cov(b,a)\right)^{0.5} \quad (7)$$

where u_{mo} is the uncertainty due to changes in output mass readings, u_a and u_b are the uncertainties of the calibration curve equation coefficients (a and b), m_o is the load cell output mass reading, and $Cov(b,a)$ is the covariance of the calibration curve coefficients.

$$u_{mo}^2 = u_m^2 + u_R^2 \quad (8)$$

$$u_m = \frac{s_m}{\sqrt{n}} \quad (9)$$

$$u_R = \frac{r}{\sqrt{3}} \quad (10)$$

Equation (8), (9), and (10) describe the uncertainty components of the mass output reading, where u_m is the standard deviation of the average measurement value, s_m is the standard deviation of repeated measurements, n is the number of repeated measurements, u_R is the uncertainty of the resolution of the data acquisition, and r is the smallest resolution value of the mass output reading. In this study, n is 10 while r is 0.1 gr.

The combined expanded uncertainty with a 95.45% confidence level for the load cell is:

$$u_{Lc} = \sqrt{(u_L^2 + u_{Dm}^2)} \quad (11)$$
$$U_{Lc} = k \times u_{Lc} \quad (12)$$

where u_L is the calibration uncertainty from Equation (7), u_{Dm} is the mass uncertainty of the mass balance (0.5%), and k is the coverage factor (value of 2). The combined uncertainty, u_{Lc}, is then determined with Equation (11). The expanded combined uncertainty, U_{Lc}, is calculated by using Equation (12) by multiply the combine uncertainty with the coverage factor. The uncertainty of the force calculation by using the load cell can be calculated by using:

$$u_F = U_{Lc} \times g \quad (13)$$
$$u_{Fr} = (u_F/F_R) \times 100\% \quad (14)$$

where u_F in Equation (13) is the force absolute uncertainty and u_{Fr} in Equation (14) is the relative uncertainty, g is the gravity acceleration of 9.81 m/s^2, and F_R is the calculated force during calibration.

B. Calibration setup and scheme

The calibration setup for the implementation of the Weighted Least Squares (WLS) method is depicted in Figure 1. It comprises a standing frame, a load cell, balance masses, a microcontroller board, and a computer as the processing unit. The standing frame measures 50 cm in length, 50 cm in width, and 60 cm in height. This setup is designed to measure the vertical force of a contraction-expansion mechanism in an underwater environment. The load cell used is a YZC-131 type, with its technical specifications listed in Table 1 [20]. The mass balance includes four 50g weights, five 100g weights, and one 200g weight. An Arduino Pro Mini serves as the microcontroller board, processing sensor data and executing programmed commands. It also facilitates communication with the computer via serial ports (UART), enabling the transfer of measured digital data and reception of commands. The HX711 module, a precision 24-bit analog-to-digital converter (ADC), is connected between the load cell and the microcontroller board, using a two-wire interface (Clock and Data).

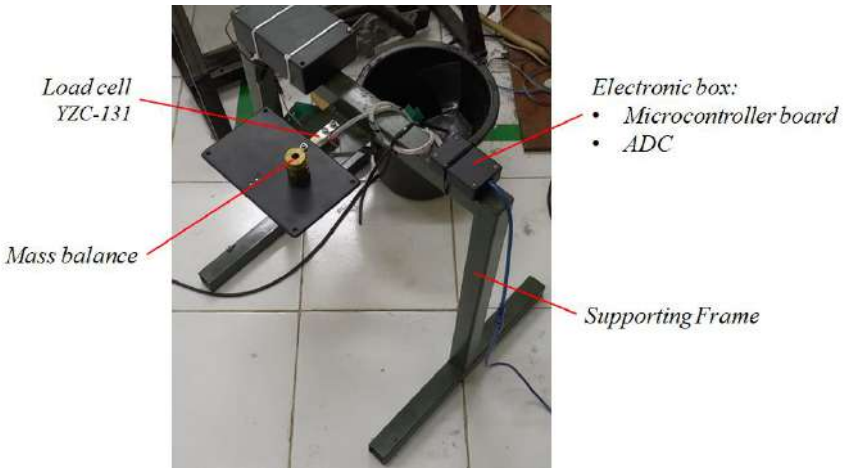

Figure 1. Calibration setup

Table 1. Specification of Load Cell Sensor YZC-131 (1 kg) [20]

Load Cell Type	Strain Gauge
Weighing Range	0 - 1 kg
Dimensions	75 mm × 12.7 mm × 12.7 mm
Precision	0.05%
Rated Output	1.0 ± 0.15 mV/V
Non-linearity	0.05% Full-Scale (FS)
Hysteresis	0.03% FS
Non-Repeatability	0.03% FS
Input Impedance	1000 ± 50 Ω
Output Impedance	1000 ± 50 Ω
Excitation Voltage	5 VDC

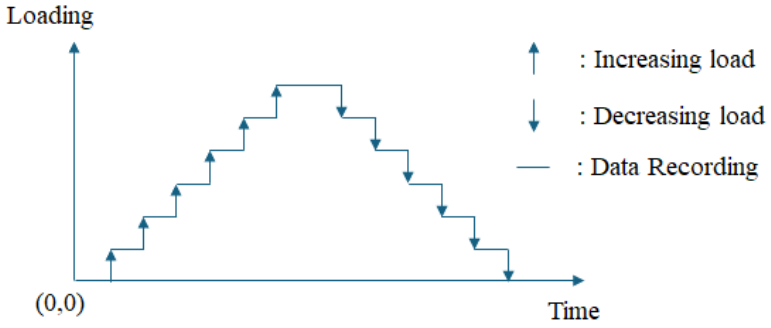

Figure 2. Calibration loading scheme

Figure 2 depicts a calibration loading scheme. It consists of three steps: increasing the load, decreasing the load, and recording the data. The sequence begins with no load (0,0), then adds a known 50 g load and measures the mass. This procedure is repeated with increasing loads until the maximum weight is attained. The load is then reduced in reverse order, with readings taken at each step. This procedure is repeated five times to ensure reliable data and high confidence in the validity of the results. Before mass calibration, the load cell was programmatically tared in accordance with the HX711 module specifications, which served as a pre-calibration step. This process produces the initial calibration factor, which is the ratio of the reading to the known weight. The pre-calibration was done with a known weight of 202.2 g, resulting in a reading of 218801 and a calibration factor of 1093.

3. Result and Discussion

Table 2 provides a detailed account of the output readings corresponding to the measured mass at various stages. The table includes data from eleven distinct stages where the load was incrementally increased and then decreased, referred to as the "Up" and "Down" loading stages. Each stage represents a specific load cycle, designed to evaluate the performance of the system under varying conditions. For each stage, the output reading is recorded, and the average value, along with the standard deviation, is calculated based on five repetitions of the loading cycles. These statistical measures, shown in the last two columns of the table, help assess the consistency and reliability of the measurement process. It is important to note that the system has already tared, ensuring that the input mass and output reading are expressed in the same unit of grams. The data reveals that the maximum standard deviation observed is 0.05 grams, a figure that predominantly appears during the initial and final stages of the loading process. This indicates that the precision of the system is slightly lower at the extremes of the loading range. The use of a single known input for the taring process may also contribute to this variability in standard deviation. The standard deviation appears to stabilize around 200g, reaching peak accuracy near 400g, before increasing again as the mass deviates further from the tared value.

Table 2. Output reading of the measured mass

No	Mass (gr)	First Loading (gr)		Second Loading (gr)		Third Loading (gr)		Fourth Loading (gr)		Fifth Loading (gr)		Average (gr)	Standard deviation (gr)
		Up	Down	Up	Down	Up	Down	Up	Down	Up	Down		
1	0	0.0	0.2	0.2	0.2	0.2	0.1	0.1	0.1	0.2	0.2	0.1	0.05
2	50.6	50.2	50.3	50.3	50.3	50.3	50.2	50.3	50.3	50.4	50.4	50.3	0.05
3	100.6	100.4	100.5	100.5	100.5	100.5	100.4	100.4	100.4	100.5	100.5	100.4	0.04
4	150.6	150.4	150.5	150.5	150.5	150.5	150.4	150.4	150.5	150.5	150.5	150.4	0.04
5	200.8	200.4	200.5	200.4	200.5	200.5	200.4	200.5	200.5	200.5	200.5	200.5	0.04
6	300.8	300.7	300.7	300.7	300.8	300.7	300.7	300.7	300.8	300.7	300.7	300.7	0.03
7	400.8	400.8	400.7	400.8	400.8	400.8	400.7	400.8	400.8	400.8	400.7	400.8	0.02
8	501	501.0	501.0	501.0	501.0	501.1	501.0	501.0	501.0	501.0	501.0	501.0	0.03
9	601	601.0	601.0	601.1	601.1	601.1	601.0	601.0	601.0	601.0	601.0	601.0	0.03
10	701.4	701.3	701.3	701.2	701.2	701.3	701.2	701.2	701.2	701.2	701.2	701.2	0.05
11	901.6	901.6	901.6	901.6	901.6	901.7	901.7	901.5	901.5	901.6	901.6	901.6	0.05

Table 3. Linear model properties

w	*X*		*Y*
0.003	336.2	44.5	0.0
0.002	434.4	21851.8	21981.7
0.001	760.2	76358.6	76474.8
0.001	793.4	119366.2	119485.6
0.002	665.8	133474.8	133699.0
0.001	914.3	274972.6	275032.8
0.001	1655.9	663613.4	663672.6
0.001	1053.4	527769.8	527750.7
0.001	1370.5	823746.2	823687.8
0.002	467.9	328093.3	328176.0
0.002	432.1	389561.4	389556.5

Table 3 illustrates the components of the linear regression model, specifically the matrix *X*, vector *Y*, and weight *w*, as derived from Equations (3), (4), and (5). The matrix *X* represents the input variables, the vector *Y* corresponds to the observed outcomes, and the weight *w* is assigned to each observation to account for its uncertainty. In this context, the weight reflects the level of confidence in each measurement, where smaller variances indicate more reliable (or certain) observations, and thus, receive smaller weights. Conversely, observations with larger variances, which are less reliable (or uncertain), are assigned larger weights. This weighting process is crucial for the Weighted Least Squares (WLS) estimation method used in this study, as it ensures that observations with higher uncertainty have a proportionately smaller influence on the final model.

Table 4 presents the key properties of the calibration curve derived from the experimental data. The intercept and slope of the calibration curve are obtained using Equation (2), while the uncertainties and covariance associated with these properties are calculated through Equation (6). These parameters define the load cell calibration equation, which is expressed as $m_C = 0.193 + 1.000\, x_c$ in units of grams, as shown in Equation (1). This equation provides a mathematical relationship between the measured output and the actual mass, allowing for accurate calibration of the load cell. The uncertainties associated with the coefficients of the linear model in the current calibration process are notably small, indicating a high degree of confidence in the accuracy and reliability of the calibration results. This precision emphasizes the effectiveness of the calibration procedure, and the robustness of the model used in this study.

Table 4. Calibration curve properties

Intercept (*b*)	0.193
Slope (*a*)	1.000
u_a	2×10^{-6}
u_b	8×10^{-4}
cov(*a*,*b*)	-1×10^{-9}

Table 5. Expanded uncertainty of the measurement

No	Massa [gr]	Output reading, m_o [gr]	u_m [gr]	u_R [gr]	u_{mo} [gr]	u_L [gr]	u_{Dm} [gr]	u_{LC} [gr]	U_{LC} [gr]
1	0.0	0.1	0.02	0.06	0.06	0.06	0.0	0.1	0.1
2	50.6	50.3	0.02	0.06	0.06	0.06	0.3	0.3	0.5
3	100.6	100.4	0.02	0.06	0.06	0.06	0.3	0.3	0.5
4	150.6	150.4	0.02	0.06	0.06	0.06	0.3	0.3	0.5
5	200.8	200.5	0.02	0.06	0.06	0.06	0.3	0.3	0.5
6	300.8	300.7	0.01	0.06	0.06	0.06	0.5	0.5	1.0
7	400.8	400.8	0.01	0.06	0.06	0.06	0.5	0.5	1.0
8	501.0	501.0	0.01	0.06	0.06	0.06	0.5	0.5	1.0
9	601.0	601.0	0.01	0.06	0.06	0.06	0.5	0.5	1.0
10	701.4	701.2	0.02	0.06	0.06	0.06	0.5	0.5	1.0
11	901.6	901.6	0.02	0.06	0.06	0.06	1.0	1.0	2.0

Table 5 provides a comprehensive summary of the expanded uncertainty calculations involved in the calibration process. The uncertainty components listed in each column are determined through a series of calculations based on Equations (7) through (12). These calculations are essential in quantifying the various sources of uncertainty that contribute to the overall measurement error. The final column of the table presents the combined expanded uncertainty U_{Lc} at a confidence level of 95.45%. A notable trend in the data is that the combined expanded uncertainty increases with the increasing input mass. This trend may be primarily attributed to the characteristics of the mass balance used in the calibration process, where the uncertainty associated with the mass measurement tends to increase as the mass itself increases. This observation suggests that the mass balance currently employed in the calibration process might benefit from future improvements, specifically targeting a

reduction in its inherent uncertainty. Ensuring that the mass balance has a very small and stable uncertainty across a wide range of masses would enhance the accuracy and reliability of the calibration.

For applications involving the measurement of force, the input and output mass readings can be converted into force measurements by multiplying by the standard acceleration due to gravity. This conversion is crucial for contexts where force, rather than mass, is the primary quantity of interest. Figure 3 illustrates the relationship between the input calibration weight and the output estimated weight as derived from the linear calibration equation. The figure demonstrates a strong agreement between the calibration data points and the estimated line of best fit P_e. This close alignment indicates that the linear model provides an accurate representation of the calibration process. The figure also includes lines representing the uncertainty bounds P_{e+} and P_{e-}, which define the range of uncertainty associated with the output estimates. It is evident from the figure that the input calibration weights consistently fall within the bounds of the output uncertainty, affirming the reliability of the calibration. Additionally, three inset figures are provided to emphasize the observed increase in uncertainty with the increasing input weight. These insets offer a more detailed view of the relationship between input weight and uncertainty, highlighting the importance of accounting for this trend in the calibration process.

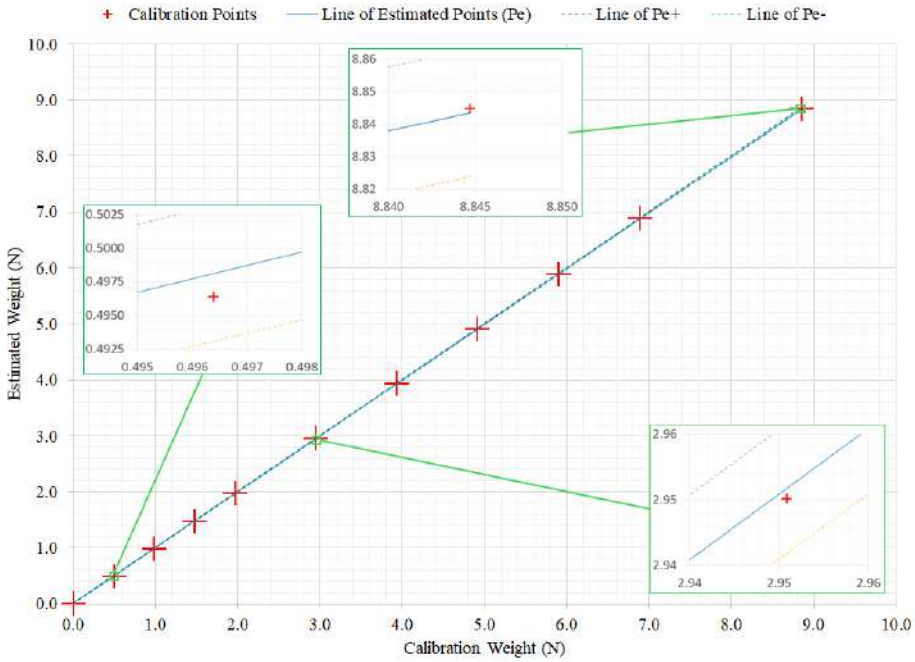

Figure 3. Calibration points and estimated curve by the model based on WLS and associated uncertainties (inset: Zoom view near the Calibration Weight of 0.496 N, 2.951 N, and 8.845 N)

The outcomes related to hysteresis, expanded uncertainty, and sensitivity of the force measurement systems are detailed in Table 6. The maximum observed hysteresis is notably small when expressed as a percentage of the Full-Scale Span (FSS) of the measurement system. This suggests that the hysteresis effect, which could potentially introduce errors into the measurements, is minimal and unlikely to significantly impact the overall accuracy of the system. However, the expanded uncertainty values exhibit a relatively higher percentage when compared to the FSS, especially in contrast to the specifications of the load cell provided in Table 1. This observation implies that the Weighted Least Squares (WLS) method employed in this study may capture a broader range of uncertainty sources, thereby offering a more realistic assessment of the performance of the measurement system. The increased uncertainty values could also serve to confirm earlier indications regarding the high uncertainty associated with the mass balance used in the current setup. This suggests that the contribution of the mass balance to the overall uncertainty is significant and should be carefully considered in future calibrations. The sensitivity of the force measurement systems, as reflected in Table 6, is relatively high, indicating that the system is highly responsive to

changes in the applied force. This high sensitivity is crucial for accurately detecting small variations in force, which is essential in precision measurement applications.

Table 6. The maximum characteristic of the force measurement system

Hysteresis (N)	Expanded Uncertainty (N)	Sensitivity
7×10^{-4} (0,008% FSS)	±0,02 (±0,2% FSS)	0.01 (N/gr)

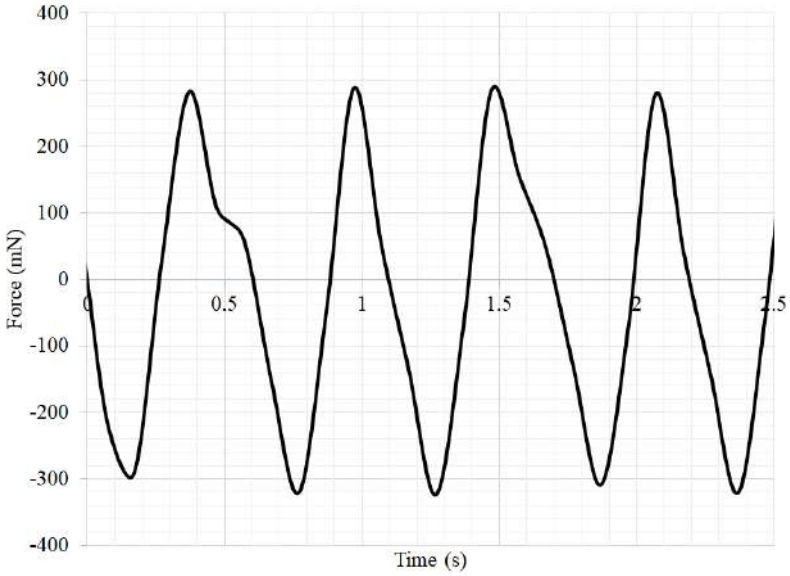

Figure 4. Continuous vertical force measurement using the present setup of calibrated systems

Figure 4 provides a sample of continuous vertical force measurements obtained using the current load cell configuration. The figure demonstrates that the present system is capable of capturing detailed and valuable information about the measured force. This capability is particularly important for applications that require precise force measurements over time. Additionally, the figure highlights specific aspects of the force measurement data that could be further analyzed for other applications. For instance, the ability of the system to measure expansion and compression forces makes it suitable for use in biomimetic models, where accurately replicating the mechanical properties of biological tissues is essential. The data captured by the system could provide insights into the behavior of such models under various force conditions, potentially leading to advancements in the design and evaluation of biomimetic systems.

4. Conclusion

This study has successfully conducted an uncertainty analysis of a measurement system using a load cell through a thorough calibration process. The Weighted Least Squares (WLS) method was employed to derive a linear calibration equation, applied to a repeated “Up” and “Down” loading scheme using a mass balance. The use of a single known input for the taring process may contribute to variations in standard deviation, with precision improving and reaching optimal performance near the tared mass. Beyond this point, the standard deviation increases as the mass diverges from the tared value, indicating the need for a more robust taring method to maintain accuracy across a wider range of measurements. The uncertainties associated with the linear curve coefficients, $u_a = 2 \times 10^{-6}$ and $u_b = 8 \times 10^{-4}$, contribute minimally to the variation in the estimated mass values, indicating the robustness of the calibration equation. However, the expanded uncertainty of the calibration process increases with the input mass, highlighting the significant impact of the inherent uncertainty of the mass balance on the overall uncertainty in the current setup. Despite this, the input calibration weight consistently falls within the estimated

weight range and its associated uncertainty. The hysteresis observed in the system, approximately 0.008% of the Full-Scale Span (FSS), is negligible and does not significantly affect the accuracy of the measurements. By accounting for uncertainties in both the measurement readings and the mass balance, the maximum combined uncertainty in this calibration process was determined to be ±0.02 N (±0.2% FSS). This value, though higher than the specified uncertainty of the load cell, is sufficient for applications requiring moderate precision. The sensitivity of the system, measured at 0.01 N/g, is adequate for detecting small fluctuations, making it particularly useful for force measurements in biomimetic models, where precise and responsive measurement systems are crucial. Future work could focus on further reducing the uncertainty of the input mass balance and incorporating environmental factors such as temperature and humidity into the uncertainty analysis. This improved setup would be highly valuable for more detailed investigations of forces in biomimetic models, potentially advancing the understanding of the field of biological systems and their mechanical properties.

Acknowledgment

The authors gratefully acknowledge the support and research facilities provided by Universitas Pertamina.

References

[1]. Y. Bar-Cohen and C. Breazeal, "Biologically Inspired Intelligent Robots," Biol. Inspired Intell. Robot., pp. 1–7, 2003, doi: 10.1117/3.2068093.

[2]. R. Wang, S. Wang, Y. Wang, L. Cheng, and M. Tan, "Development and Motion Control of Biomimetic Underwater Robots: A Survey," IEEE Trans. Syst. Man, Cybern. Syst., vol. 52, no. 2, pp. 833–844, Feb. 2022, doi: 10.1109/TSMC.2020.3004862.

[3]. K. Bu, X. Gong, C. Yu, and F. Xie, "Biomimetic Aquatic Robots Based on Fluid-Driven Actuators: A Review," *Journal of Marine Science and Engineering*, vol. 10, no. 6. MDPI, Jun. 01, 2022. doi: 10.3390/jmse10060735.

[4]. A. S. Jaya and M. W. Kartidjo, "Thrust and efficiency enhancement scheme of the fin propulsion of the biomimetic Autonomous Underwater Vehicle model in low-speed flow regime," Ocean Eng., vol. 243, Jan. 2022, doi: 10.1016/j.oceaneng.2021.110090.

[5]. A. S. Jaya, M. W. Kartidjo, B. W. Riyandwita, and Y. F. Buys, "Transition phase in the static thrust generation of the biomimetic fin with low oscillating frequency," Eng. Res. Express, vol. 5, no. 3, p. 035055, Sep. 2023, doi: 10.1088/2631-8695/acf275.

[6]. G. Li, G. Liu, D. Leng, X. Fang, G. Li, and W. Wang, "Underwater Undulating Propulsion Biomimetic Robots: A Review," Biomimetics, vol. 8, no. 3, 2023, doi: 10.3390/biomimetics8030318.

[7]. D. J. Callaghan, M. M. Mcgrath, and E. Coyle, "Force Measurement Methods in Telerobotic Surgery : Implications for End-Effector Manufacture," Proc. 25th Int. Manuf. Conf., pp. 389–398, 2008, doi: 10.21427/D7889V.

[8]. T. Shahid, D. Gouwanda, S. G. Nurzaman, and A. A. Gopalai, "Moving toward soft robotics: A decade review of the design of hand exoskeletons," Biomimetics, vol. 3, no. 3, 2018, doi: 10.3390/biomimetics3030017.

[9]. Q. Fu, H. C. Astley, and C. Li, "Snakes combine vertical and lateral bending to traverse uneven terrain," Bioinspir. Biomim., vol. 17, pp. 1–37, 2022, doi: 10.1088/1748-3190/ac59c5.

[10]. S. A. Brooks, J. D. Brooks, and M. A. Green, "Force measurements near a natural frequency of a measurement system using inverse filters," Meas. Sci. Technol., vol. 33, no. 2, 2022, doi: 10.1088/1361-6501/ac3943.

[11]. T. Bartel, "Uncertainty in NIST force measurements," J. Res. Natl. Inst. Stand. Technol., vol. 110, no. 6, pp. 589–603, 2005, doi: 10.6028/jres.110.084.

[12]. A. P. Singh, S. K. Ghoshal, H. Kumar, J. Yoon, and P. Yadav, "Development and Metrological Evaluation of a Force Transducer for Industrial Application," IEEE Access, vol. 9, pp. 33299–33312, 2021, doi: 10.1109/ACCESS.2021.3060746.

[13]. R. C. Hurley, "Stress and force measurement uncertainties in 3D granular materials," Powders Grains 2021 - 9th Int. Conf. Micromechanics Granul. Media, vol. 02009, pp. 1–4, 2021, doi: 10.1051/epjconf/202124902009.

[14]. M. Emmanouil and B. Vassilis, "Uncertainty and traceability in calibration by comparison," Meas. Sci. Technol., vol. 11, p. 771, 2000, [Online]. Available: http://stacks.iop.org/0957-0233/11/i=6/a=321

[15]. J. L. Ferreira *et al.*, "Application of weighted least squares to calibrate a digital system for measuring the respiratory pressures," BIODEVICES 2008 - Proc. 1st Int. Conf. Biomed. Electron. Devices, vol. 1, no. figure 1, pp. 220–223, 2008.
[16]. A. S. Jaya, M. W. Kartidjo, L. R. Zuhal, and I. S. Brodjonegoro, "Evaluation of force and torque measurement uncertainties of the three-component dynamometer of the biomimetic fin propulsion system," pp. 185–190, 2018.
[17]. L. Maybank, A. Knott, and D. Elkington, "Guide to the Uncertainty of Force Measurement," no. April, 1999.
[18]. J. C. F. G. I. Metrology, "Evaluation of measurement data — Guide to the expression of uncertainty in measurement," Int. Organ. Stand. Geneva ISBN, vol. 50, no. September, p. 134, 2008, [Online]. Available: http://www.bipm.org/en/publications/guides/gum.html
[19]. Euromet cg-4, "Uncertainty of Force Measurements Calibration Guide Version 2.0," 2011.
[20]. "YZC-131A Load Cells." [Online]. Available: https://www.electronicoscaldas.com/datasheet/YZC-131A.pdf

Biographies of Authors

Muhammad Farhan graduated in 2023 with a Sarjana Teknik degree from the Department of Mechanical Engineering at Universitas Pertamina. He is currently employed as an engineer at a private company in Jakarta.

Arie Sukma Jaya is a lecturer in the Department of Mechanical Engineering at the Faculty of Industrial Technology, Universitas Pertamina. His research interests include biomimetic robots and unmanned vehicles.

Vol. 03, No. 2, December 2024, pp. 79-91
p-ISSN: 2963-8577
e-ISSN: 2964-3511
DOI: 10.57102/jescee.v3i2.88

ANALYSIS OF THE EFFECT OF LOAD CHANGES ON THE PERFORMANCE OF SYNCHRONOUS GENERATOR UNIT 2 AT PT. PLN NUSA DAYA UNIT PLTU MALINAU

Andri[1*], Ismit Mado[1], Muhammad Arif [2], Ferry K. Maring[2]
[1]Department of Electrical Engineering, Faculty of Engineering, University of Borneo Tarakan, North Kalimantan, Indonesia
[2]PT.PLN Nusa Daya Unit PLTU Malinau, Malinau City, North Kalimantan, Indonesia

Abstract
Changes in generator power losses are adjusted to the load needs in the field, which is constantly changing and can affect the value of the per-phase current and generator field current, causing power losses. The resulting power losses affect the efficiency of the PLTU generator. To determine the generator's efficiency due to load changes, this study was carried out using manual calculation method by collecting data on specifications, resistance, and dialy log sheets of the 2x3 MW Malinau PLTU generator unit 2 conducted at PT. Nusa Daya Unit PLTU Malinau. Based on the callculation data on May 17, the highest efficiency was 79,69% at a load 2,372 MW, while the lowest efficiency was 78,03% at a load of 2,137 MW. For the callculation results of May 18, the highets efficiency was 79,51% at a load 2,342 MW, while the lowest efficiency was 76,37% at a load of 1,941 MW. The greater the power generated by generator, the higher the efficiency of the generator and the better the generator performance.

Keywords:
PLTU; generator; load changes; power losses; efficiency

Article History:
Received: August 26th, 2024
Revised: December 11th, 2024
Accepted: December 12th, 2024
Published: December 13rd, 2024

Corresponding Author:
Andri
Department of Electrical Engineering, Universitas Borneo Tarakan, Indonesia
Email: Andri887654@gmail.com

1. Introduction

The need for electrical energy is one of the basic needs in human life today. Electrical energy produced from power plants supports human activities, including needs for industrial activities, commercial activities and people's daily life activities that must be met. The use of electrical energy isin many ways, such as lighting sources, power sources for electrical equipment, even power sourcesfor electric vehicles and the use of this electrical energy will increase every year, thereby encouragingthe electric power system to operate optimally.

PT National Electric Service Nusa Daya (PT PLN ND) is a company providing operation and maintenanceservices for power plants under 100 MW, having one of the Malinau sector plants, namely a PLTU with a capacityof 2x3 MW using coal as fuel. A steam power plant (PLTU) is a type of generator that utilizes steam (steam) fromthe results of combustion on boiler to drive a turbine which is coupled directly to a generator so that the generatorcan produce electrical energy, therefore the generator is an important component in the generating system. Efficiency of the generator greatly influences the performance of the power generation system, the greater the efficiency of thegenerator, the better the reliability of the system. The decrease in generator efficiency values occurs due to severalfactors such as generator power losses, generator trips (units shutdown), and duration of maintenance.

The power generated by the generator is adjusted to the load demand, the load received by the generatoralways changes depending on field conditions, because changes in load will result in power losses which greatlyaffect the efficiency of the generator [1].

When the electrical load changes (fluctuations), it will affect the performance of a generator. As theelectricity demand increases and the load generated increases, the generator work decreases [2].

The performance of a synchronous generator is measured by calculating efficiency, namely the comparisonbetween the generator's input and output power. If the generator operates with an efficiency below 80%, theenergy supplied is not optimal because a lot of electrical energy is lost due to losses [3].

In electrical energy generation systems, especially in synchronous generators, the generator is operated at aload that varies over time which causes instability in the generator's performance, the load changes that occur aredue to the use of electrical loads. The result of generator performance that is not optimal is that it can cause adecrease in the performance of the PLTU's electrical power system. In this research, we will analyze the effect ofload changes on the performance of generator unit 2 (two) at PLTU 2x3 MW Malinau. Some data is needed suchas specification data, obstacles, etc logsheet daily generator.

2. Method

A. Electric Power

The power triangle is the relationship between active power, reactive power and apparent power that can be expressed by representing these powers as vectors. The formula for power in a 3-phase triangular circuit is as follows [4].

$$P = \sqrt{3}\, V_L\, I_L \cos\varphi \quad (1)$$

$$Q = \sqrt{3}\, V_L\, I_L \sin\varphi \quad (2)$$

$$S = \sqrt{3}\, V_L\, I_L \quad (3)$$

With:

P = Active power (Watt)

Q = Reactive power(VAR)

S = Apparent power(VA)

V_L = 3-phase power (Volt)

I_L = 3-phase current (Ampere)

φ = power factor

B. Synchronous Generator Losses

Power losses consist of no-load losses and also copper losses, and to calculate these power losses use the following equation [1].

Loss without load:

$$Loss\ wihtout = Vt\ x\ If \quad (4)$$

With:

Vt = Terminal voltage (Volt)

If = Field current (Ampere)

Electrical or Copper Losses:

1. Stator Winding Losses

This loss is the ohm loss that occurs in the stator winding which can be calculated using Eq.

$$Pcu\ jangkar = 3\ Ia^2\ x\ Ra \quad (5)$$

With:

P*cu anchor* = Stator copper loss (Watt)

Ia = Current in the stator (Ampere)

Ra = Stator resistance (Ω)

2. Rotor Winding Losses

Rotor winding losses referred to as energy losses in the field coil can be calculated using Eq.

$$Pcu\ medan = I_f^2 \text{ x } R_f \quad (6)$$

With:

Pcu *filed* = Rotor copper loss (Watt)
If = Current flow in the rotor winding (Ampere)
Rf = Resistance of the rotor (Ω)

So the total power loss in the generator is as in the equation:

$$\Sigma Prugi = No\text{-}load\ lass + anchor\ Pcu + filed\ Pcu \quad (7)$$

C. Synchronous Generator Efficiency

Generator efficiency is the comparison between output power and input power. As is the case with other electrical machines and transformers, the efficiency of a synchronous generator can be written as below [5].

$$\eta = \frac{Pout}{Pin} \text{ x } 100\% \quad (8)$$

$$Pin = Pout + \Sigma Prugi \quad (9)$$

With:

η = Generator efficiency
Pin = Input power (Watt)
Pout = Output power (Watt)

Generator efficiency is the ratio between the output power value and the generator input power value in MW units and is expressed in the form of a percent (%). In synchronous generators, the generator efficiency value is greatly influenced by power losses, therefore the input power is determined from the output power plus the total power losses.

D. Generator Unit 2 Generator Unit 2 Specification and Resistance Data

Specifications for generator unit 2 of PLTU Nusa Daya 2x3 MW Malinau are as in table 1.

Table 1. Generator Specification and Resistance Data

Manufactur	Luoyang Generating
Model	QFK-K3 5-2
Voltage	6,3 kV
Rated Power	3,5 MW
Rated Current	377 A
Rated Speed	3000 r/min
Rated Frequency	50 Hz
Capacity	4,118 MVA
Rated Field Voltage	77 V
Rated Field Current	239 A
Exciting current at no-load	93 A
Power Factor/Cos φ	0,85
Phase/Connected	3/Y

Efifciency	96,8 %
Resistance Stator	0,066 Ω
Resistance Rotor	0,268 Ω

E. Unit 2 Generator Loading Data

Data retrieval *logsheet* generator unit 2 was carried out for 2 days starting 17-18 May 2024. The data was obtained from the CCR room (*Central Control Room*) PLTU Nusa Daya and known parameters as in table 2 to table 3.

Table 2. Load 17 May 2024

Time	Actual Load		Frequency (Hz)	Output Voltage (kV)			*Cos φ*	Current (A)			Filed Current (If)
	MW	kVAR		R	S	T		R	S	T	
01:02	2,338	753	50.16	6,286	6,385	6,219	0,94	213	216	215	154
02:02	2,332	762	50.15	6,286	6,384	6,217	0,94	209	212	213	154
03:02	2,333	788	50.15	6,289	6,379	6,218	0,94	209	214	213	155
04:02	2,336	758	50.15	6,286	6,382	6,237	0,94	212	216	215	156
05:02	2,304	757	50.16	6,284	6,381	6,211	0,94	209	214	214	154
06:02	2,302	739	50.15	6,282	6,380	6,210	0,94	209	212	211	155
07:02	2,343	881	50.15	6,281	6,380	6,211	0,93	212	215	217	156
08:02	2,503	932	50.13	6,282	6,382	6,205	0,92	222	225	227	160
09:02	2,171	960	50.15	6,282	6,382	6,208	0,91	217	221	222	159
10:02	2,335	1,246	50.18	6,283	6,382	6,207	0,88	242	244	246	160
11:02	2,341	1,271	50.15	6,285	6,386	6,207	0,89	244	243	245	162
12:02	2,334	1,138	50.17	6,281	6,384	6,212	0,89	236	238	240	162
13:02	2,324	1,129	50.15	6,282	6,386	6,209	0,90	236	238	238	162
14:02	2,343	1,271	50.15	6,285	6,386	6,207	0,89	244	243	245	162
15:02	2,381	1,201	50.17	6,282	6,384	6,214	0,89	241	244	248	163
16:02	2,332	1,089	50.15	6,281	6,383	6,213	0,90	240	242	243	161
17:02	2,375	1,107	50.16	6,282	6,384	6,211	0,90	238	239	241	162
18:02	2,308	907	50.16	6,289	6,382	6,215	0,92	225	226	228	160
19:02	2,328	770	50.17	6,285	6,383	6,215	0,94	212	214	214	161
20:02	2,329	858	50.16	6,288	6,382	6,216	0,92	211	214	214	161
21:02	2.201	802	50.14	6,290	6,382	6,218	0,94	212	215	216	158
22:02	2.202	762	50.17	6,290	6,385	6,218	0,94	211	212	213	157
23:02	2.347	804	50.16	6,290	6,385	6,220	0,94	213	216	216	157
00:02	2.315	761	50.16	6,287	6,385	6,218	0,94	211	213	213	155

Table 3. Load 18 May 2024

Time	Actual Load		Frequency (Hz)	Output Voltage (kV)			*Cos φ*	Current (A)			Field Current (If)
	MW	kVAR		R	S	T		R	S	T	
01:02	2,273	795	50.16	6,293	6,380	6,227	0,94	220	223	222	153
02:02	2,265	849	50.17	6,274	6,383	6,194	0,93	220	224	223	152
03:02	2,257	798	50.16	6,249	6,374	6,189	0,93	219	221	223	151
04:02	2,269	796	50.18	6,273	6,382	6,194	0,94	217	221	220	152
05:02	2,252	754	50.14	6,284	6,383	6,211	0,95	215	218	218	151
06:02	2,249	810	50.15	6,282	6,380	6,209	0,94	218	221	221	150
07:02	2,268	792	50.17	6,283	6,382	6,211	0,94	216	219	220	152
08:02	2,277	865	50.14	6,208	6,380	6,246	0,93	218	222	223	154
09:02	2,285	1,025	50.15	6,281	6,380	6,203	0,91	227	231	232	156
10:02	2,232	1,170	50.14	6,280	6,384	6,205	0,88	230	232	232	156
11:02	2,009	1,106	50.21	6,287	6,385	6,216	0,86	206	208	207	154

12:02	1,990	1,180	50.16	6,287	6,382	6,220	0,85	210	213	212	152
13:02	2,177	1,031	50.15	6,285	6,383	6,217	0,90	218	220	221	153
14:02	2,251	1,181	50.16	6,283	6.383	6,216	0,88	233	235	235	154
15:02	2,236	1,223	50.15	6,274	6,385	6,192	0,87	234	237	237	154
16:02	2,245	1,167	50.17	6,267	6,385	6,192	0,88	233	235	234	154
17:02	2,360	1,155	50.14	6,269	6,381	6,194	0,89	240	242	242	158
18:02	2,353	1,006	50.16	6,267	6,378	6,193	0,91	234	237	239	156
19:02	2,395	933	50.17	6,273	6,381	6,191	0,93	226	229	232	161
20:02	2,330	1,155	50.14	6,269	6,381	6,194	0,89	240	242	242	160
21:02	2,274	877	50.19	6,272	6,386	6,191	0,93	220	222	224	160
22:02	2,263	854	50.16	6,294	6,384	6,191	0,93	220	223	223	158
23:02	2,287	834	50.16	6,296	6,381	6,232	0,94	219	222	222	156
00:02	2,238	803	50.14	6,289	6,383	6,222	0,94	218	221	220	154

3. Results and Discussion

A. *Generator Unit 2 Power Calculation*

Calculation of the output power of a 3-phase generator is done by calculating the average voltage and average current. Some of the data used in the calculations are voltage (kV), three-phase current (A), and power factor (cos φ). So the calculated output power is obtained using the equation:

- *Avarage V* $= V_R + V_S + V_T$

  $= 6{,}286 + 6{,}385 + 6{,}219$

  $= 18{,}890$ kV

  $= \frac{18{,}900}{3} = 6{,}297$ kV

- *Avarage I* $= I_R + I_S + I_T$

  $= 213 + 216 + 215$

  $= \frac{644}{3} = 214{,}67\ A$

- *Pout* $= \sqrt{3}\ V_L\ I_L \cos\varphi$

  $= \sqrt{3}$ x 6,297 x 214,67 x 0,94

  = 2,200 MW

B. *Generator Unit 2 Power Losses*

To find out the generator efficiency value, first calculate the power losses on the generator by calculating the no-load loss and copper losses (anchor and field) on the loading data for May 17 and 18. Some data used in calculations such as output voltage (Vt), field current (If), generator stator and rotor resistance (Ω), armature and field current (A) are obtained from generator specifications, *logsheet* daily generator, and *manual book*.

No-Load Loss:

- *Pno-load* $= Vt \times If$

  = 6.300 x 93

  = 585.900 Watt

  = 0,5859 MW

Copper Loss Calculation:

- *R phase anchor Pcu* = Ia^2 x *Ra*
  = 213^2 x 0,066
  = 2.994,35 Watt
  = 0,00299 MW
- *S phase anchor Pcu* = Ia^2 x *Ra*
  = 216^2 x 0,066
  = 3.079,30 Watt
  = 0,00308 MW
- *T phase anchor Pcu* = Ia^2 x *Ra*
  = 215^2 x 0,066
  = 3.050,85 Watt
  = 0,00305 MW
- *Σ anchor Pcu* = 0,00299 + 0,00308 + 0,00305
  = 0,00912 MW
- *Field Pcu* = If^2 x *Rf*
  = 154^2 x 0,268
  = 6.355,89 Watt
  = 0,00636 MW

Based on the calculation results above, the total power losses are obtained using the equation:

- Σ*Ploss* = *No-load loss* + *Σ anchorPcu* + *Field Pcu*
  = 0,5859 + 0,00912 + 0,00636
  = 0,601 MW

C. Calculation of Generator Efficiency Unit 2

Generator efficiency calculations are carried out starting from the parameters *Pout* (MW) the calculation results are added to *ΣPloss* to gain value *Pin* (MW). Then assess *Pin* is entered into the generator efficiency equation, then the percentage of generator efficiency in the loading data is as follows:

Pin = *Pout* + *ΣPloss*

Pin = 2,200 + 0,600

= 2,800 MW

$\eta\ (gen) = \frac{Pout}{Pin}$ x 100%

$\eta = \frac{2,200}{2,800}$ x 100%

= 79,58 %

D. Tables and Figure

The results of the calculation of electrical power, total losses and generator efficiency are presented in the form of tables and graphs and then analyzed the effect of load changes on the performance of the synchronous generator as measured by the efficiency value.

Table 4. Power Calculation Results 17 May 2024

Time	Actual Data								Calculation Data		
	Pout (MW)	Output Voltage (kV)			Current (A)			*Cos φ*			
		R	S	T	R	S	T		Avarage V (kV)	Avarage A (I)	*Pout* (MW)
01:02	2,338	6,286	6,385	6,219	213	216	215	0,94	6,297	214,67	2,200
02:02	2,332	6,286	6,384	6,217	209	212	213	0,94	6,296	211,33	2,166
03:02	2,333	6,289	6,379	6,218	209	214	213	0,94	6,295	212,00	2,173
04:02	2,336	6,286	6,382	6,237	212	216	215	0,94	6,302	214,33	2,197
05:02	2,304	6,284	6,381	6,211	209	214	214	0,94	6,292	212,33	2,176
06:02	2,302	6,282	6,380	6,210	209	212	211	0,94	6,291	210,67	2,159
07:02	2,343	6,281	6,380	6,211	212	215	217	0,93	6,291	214,67	2,177
08:02	2,503	6,282	6,382	6,205	222	225	227	0,92	6,290	224,67	2,254
09:02	2,171	6,282	6,382	6,208	217	221	222	0,91	6,291	220,00	2,183
10:02	2,335	6,283	6,382	6,207	242	244	246	0,88	6,291	244,00	2,341
11:02	2,341	6,285	6,386	6,207	244	243	245	0,89	6,293	244,00	2,368
12:02	2,334	6,281	6,384	6,212	236	238	240	0,89	6,292	238,00	2,310
13:02	2,324	6,282	6,386	6,209	236	238	238	0,90	6,292	237,33	2,329
14:02	2,343	6,285	6,386	6,207	244	243	245	0,89	6,293	244,00	2,368
15:02	2,381	6,282	6,384	6,214	241	244	248	0,89	6,293	244,33	2,371
16:02	2,332	6,281	6,383	6,213	240	242	243	0,90	6,292	241,67	2,372
17:02	2,375	6,282	6,384	6,211	238	239	241	0,90	6,292	239,33	2,349
18:02	2,308	6,289	6,382	6,215	225	226	228	0,92	6,295	226,33	2,270
19:02	2,328	6,285	6,383	6,215	212	214	214	0,94	6,294	213,33	2,186
20:02	2,329	6,288	6,382	6,216	211	214	214	0,92	6,295	213,00	2,137
21:02	2,201	6,290	6,382	6,218	212	215	216	0,94	6,297	214,33	2,197
22:02	2,202	6,290	6,385	6,218	211	212	213	0,94	6,298	212,00	2,173
23:02	2,347	6,290	6,385	6,220	213	216	216	0,94	6,298	215,00	2,204
00:02	2,315	6,287	6,385	6,218	211	213	213	0,94	6,297	212,33	2,176

Table 5. Power Calculation Results 18 May 2024

Time	Actual Data								Calculation Data		
	Pout (MW)	Output Voltage (kV)			Current (A)			Cos *φ*			
		R	S	T	R	S	T		Avarage V (kV)	Avarage A (I)	*Pout* (MW)
01:02	2,273	6,293	6,380	6,227	220	223	222	0,94	6,300	221,67	2,273
02:02	2,265	6,274	6,383	6,194	220	224	223	0,93	6,284	222,33	2,250
03:02	2,257	6,249	6,374	6,189	219	221	223	0,93	6,271	221,00	2,232
04:02	2,269	6,273	6,382	6,194	217	221	220	0,94	6,283	219,33	2,243
05:02	2,252	6,284	6,383	6,211	215	218	218	0,95	6,293	217,00	2,246
06:02	2,249	6,282	6,380	6,209	218	221	221	0,94	6,290	220,00	2,253
07:02	2,268	6,283	6,382	6,211	216	219	220	0,94	6,292	218,33	2,236
08:02	2,277	6,208	6,380	6,246	218	222	223	0,93	6,278	221,00	2,234
09:02	2,285	6,281	6,380	6,203	227	231	232	0,91	6,288	230,00	2,279
10:02	2,232	6,280	6,384	6,205	230	232	232	0,88	6,290	231,33	2,217
11:02	2,009	6,287	6,385	6,216	206	208	207	0,86	6,296	207,00	1,941
12:02	1,990	6,287	6,382	6,220	210	213	212	0,85	6,296	211,67	1,962
13:02	2,177	6,285	6,383	6,217	218	220	221	0,90	6,295	219,67	2,155
14:02	2,251	6,283	6.383	6,216	233	235	235	0,88	6,294	234,33	2,247
15:02	2,236	6,274	6,385	6,192	234	237	237	0,87	6,284	236,00	2,234
16:02	2,245	6,267	6,385	6,192	233	235	234	0,88	6,281	234,00	2,240
17:02	2,360	6,269	6,381	6,194	240	242	242	0,89	6,281	241,33	2,336
18:02	2,353	6,267	6,378	6,193	234	237	239	0,91	6,279	236,67	2,342

19:02	2,395	6,273	6,381	6,191	226	229	232	0,93	6,282	229,00	2,317
20:02	2,330	6,269	6,381	6,194	240	242	242	0,89	6,281	241,33	2,336
21:02	2,274	6,272	6,386	6,191	220	222	224	0,93	6,283	222,00	2,246
22:02	2,263	6,294	6,384	6,191	220	223	223	0,93	6,290	222,00	2,249
23:02	2,287	6,296	6,381	6,232	219	222	222	0,94	6,303	221,00	2,267
00:02	2,238	6,289	6,383	6,222	218	221	220	0,94	6,298	219,67	2,252

Table 6. Generator Power Losses 17 May 2024

Time	Pno-load (MW)	Anchor Pcu (MW)			Field Current (If)	ΣPloss (MW)
		R	S	T		
01:02	0,5859	0,00299	0,00308	0,00305	0,00636	0,601
02:02	0,5859	0,00288	0,00297	0,00299	0,00636	0,601
03:02	0,5859	0,00288	0,00302	0,00299	0,00644	0,601
04:02	0,5859	0,00297	0,00308	0,00305	0,00652	0,602
05:02	0,5859	0,00288	0,00302	0,00302	0,00636	0,601
06:02	0,5859	0,00288	0,00297	0,00294	0,00644	0,601
07:02	0,5859	0,00297	0,00305	0,00311	0,00652	0,602
08:02	0,5859	0,00325	0,00334	0,00340	0,00686	0,603
09:02	0,5859	0,00311	0,00322	0,00325	0,00678	0,602
10:02	0,5859	0,00387	0,00393	0,00399	0,00686	0,605
11:02	0,5859	0,00393	0,00390	0,00396	0,00703	0,605
12:02	0,5859	0,00368	0,00374	0,00380	0,00703	0,604
13:02	0,5859	0,00368	0,00374	0,00374	0,00703	0,604
14:02	0,5859	0,00393	0,00390	0,00396	0,00703	0,605
15:02	0,5859	0,00383	0,00393	0,00406	0,00712	0,605
16:02	0,5859	0,00380	0,00387	0,00390	0,00695	0,604
17:02	0,5859	0,00374	0,00377	0,00383	0,00703	0,604
18:02	0,5859	0,00334	0,00337	0,00343	0,00686	0,603
19:02	0,5859	0,00297	0,00302	0,00302	0,00695	0,602
20:02	0,5859	0,00294	0,00302	0,00302	0,00695	0,602
21:02	0,5859	0,00297	0,00305	0,00308	0,00669	0,602
22:02	0,5859	0,00294	0,00297	0,00299	0,00661	0,601
23:02	0,5859	0,00299	0,00308	0,00308	0,00661	0,602
00:02	0,5859	0,00294	0,00299	0,00299	0,00644	0,601

Table 7. Generator Power Losses 18 May 2024

Time	Pno-load (MW)	Anchor Pcu (MW)			Filed Current (If)	ΣPloss (MW)
		R	S	T		
01:02	0,5859	0,00319	0,00328	0,00325	0,00627	0,602
02:02	0,5859	0,00319	0,00331	0,00328	0,00619	0,602
03:02	0,5859	0,00317	0,00322	0,00328	0,00611	0,602
04:02	0,5859	0,00311	0,00322	0,00319	0,00619	0,602
05:02	0,5859	0,00305	0,00314	0,00314	0,00611	0,601
06:02	0,5859	0,00314	0,00322	0,00322	0,00603	0,602
07:02	0,5859	0,00308	0,00317	0,00319	0,00619	0,602
08:02	0,5859	0,00314	0,00325	0,00328	0,00636	0,602
09:02	0,5859	0,00340	0,00352	0,00355	0,00652	0,603
10:02	0,5859	0,00349	0,00355	0,00355	0,00652	0,603
11:02	0,5859	0,00280	0,00286	0,00283	0,00636	0,601
12:02	0,5859	0,00291	0,00299	0,00297	0,00619	0,601
13:02	0,5859	0,00314	0,00319	0,00322	0,00627	0,602
14:02	0,5859	0,00358	0,00364	0,00364	0,00636	0,603
15:02	0,5859	0,00361	0,00371	0,00371	0,00636	0,603
16:02	0,5859	0,00358	0,00364	0,00361	0,00636	0,603
17:02	0,5859	0,00380	0,00387	0,00387	0,00669	0,604
18:02	0,5859	0,00361	0,00371	0,00377	0,00652	0,604
19:02	0,5859	0,00337	0,00346	0,00355	0,00695	0,603
20:02	0,5859	0,00380	0,00387	0,00387	0,00686	0,604
21:02	0,5859	0,00319	0,00325	0,00331	0,00686	0,603
22:02	0,5859	0,00319	0,00328	0,00328	0,00669	0,602
23:02	0,5859	0,00317	0,00325	0,00325	0,00652	0,602
00:02	0,5859	0,00314	0,00322	0,00319	0,00636	0,602

Table 8. Generator Efficiency 17 May 2024

Time	*Pout* (MW)	*ΣP*loss (MW)	*Pin* (MW)	Efficiency (%)
01:02	2,200	0,601	2,801	78,53 %
02:02	2,166	0,601	2,767	78,28 %
03:02	2,173	0,601	2,774	78,33 %
04:02	2,197	0,602	2,799	78,51 %
05:02	2,176	0,601	2,777	78,35 %
06:02	2,159	0,601	2,760	78,22 %
07:02	2,177	0,602	2,779	78,35 %
08:02	2,254	0,603	2,857	78,90 %
09:02	2,183	0,602	2,785	78,38 %
10:02	2,341	0,605	2,946	79,48 %
11:02	2,368	0,605	2,973	79,66 %
12:02	2,310	0,604	2,914	79,27 %
13:02	2,329	0,604	2,933	79,40 %
14:02	2,368	0,605	2,973	79,66 %
15:02	2,371	0,605	2,976	79,67 %
16:02	2,372	0,604	2,976	79,69 %
17:02	2,349	0,604	2,953	79,54 %
18:02	2,270	0,603	2,873	79,01 %
19:02	2,186	0,602	2,788	78,41 %
20:02	2,137	0,602	2,739	78,03 %
21:02	2,197	0,602	2,799	78,50 %
22:02	2,173	0,601	2,774	78,32 %
23:02	2,204	0,602	2,806	78,56 %
00:02	2,176	0,601	2,777	78,35 %

Table 9. Generator Efficiency 18 May 2024

Time	*Pout* (MW)	*ΣP*loss (MW)	*Pin* (MW)	Efficiency (%)
01:02	2,273	0,602	2,875	79,06 %
02:02	2,250	0,602	2,852	78,90 %
03:02	2,232	0,602	2,834	78,77 %
04:02	2,243	0,602	2,845	78,85 %
05:02	2,246	0,601	2,847	78,88 %
06:02	2,253	0,602	2,855	78,93 %
07:02	2,236	0,602	2,838	78,80 %
08:02	2,234	0,602	2,836	78,77 %
09:02	2,279	0,603	2,882	79,08 %
10:02	2,217	0,603	2,820	78,62 %
11:02	1,941	0,601	2,542	76,37 %
12:02	1,962	0,601	2,563	76,55 %
13:02	2,155	0,602	2,757	78,17 %
14:02	2,247	0,603	2,850	78,84 %
15:02	2,234	0,603	2,837	78,74 %
16:02	2,240	0,603	2,843	78,79 %
17:02	2,336	0,604	2,940	79,45 %
18:02	2,342	0,604	2,946	79,51 %
19:02	2,317	0,603	2,920	79,34 %
20:02	2,336	0,604	2,940	79,45 %
21:02	2,246	0,603	2,849	78,85 %
22:02	2,249	0,602	2,851	78,87 %
23:02	2,267	0,602	2,869	79,01 %
00:02	2,252	0,602	2,854	78,91 %

p-ISSN: 2963-8577
e-ISSN: 2964-3511

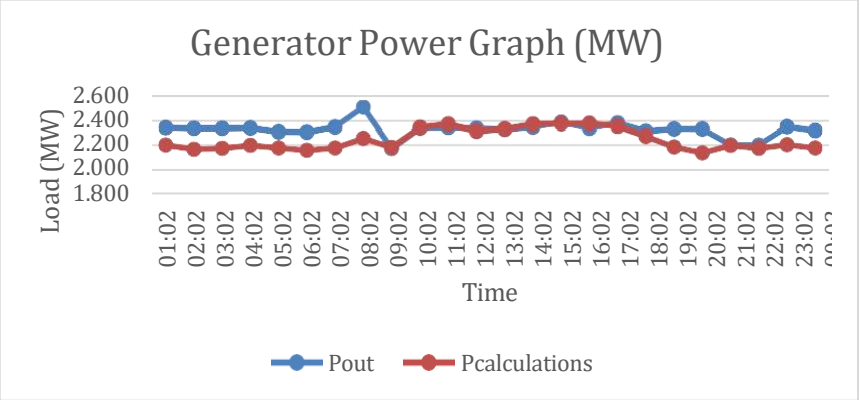

Figure 1. Actual Power Graph and Generator Calculations 17 May 2024

In Figure 1, the graph also shows changes in the generator load each hour which are not very significant with the highest load at 2,395 MW at 19:02 while the lowest load is 1,990 MW at 12:02. From the comparison graph above, it can be seen that the calculated power of the generator is very close to the value of the generator output power (Pout) at *logsheet*.

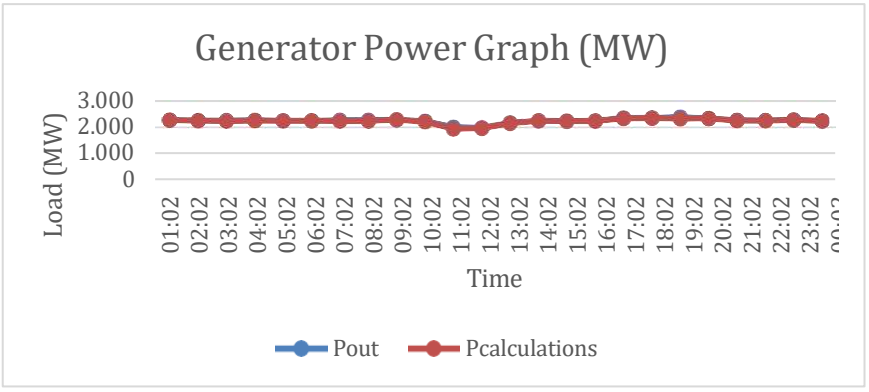

Figure 2. Actual Power Graph and Generator Calculations 18 May 2024

In Figure 2, the graph also shows changes in the generator load each hour which are not very significant with the highest load at 2,395 MW at 19:02 while the lowest load is 1,990 MW at 12:02. From the comparison graph above, it can be seen that the calculated power of the generator is very close to the value of the generator output power (Pout) at *logsheet*.

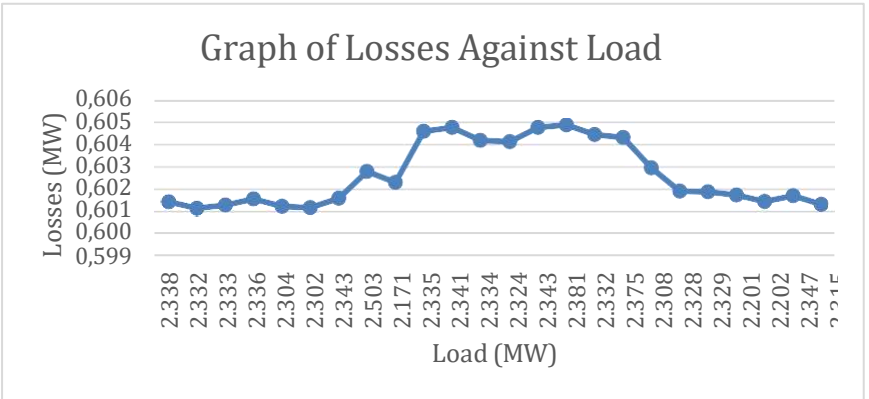

Figure 3. Graph of Losses Against Load 17 May 2024

In graph 3 of the calculation results on May 17, it can be seen that generator power losses at certain loads and times have changed. The value of power losses is influenced by phase current (A) and field current (If) due to changes in load. Based on graph 3, the highest power loss is 0.605 MW at a load of 2.381 MW, while the lowest power loss is 0.601 MW at a load of 2.332 MW.

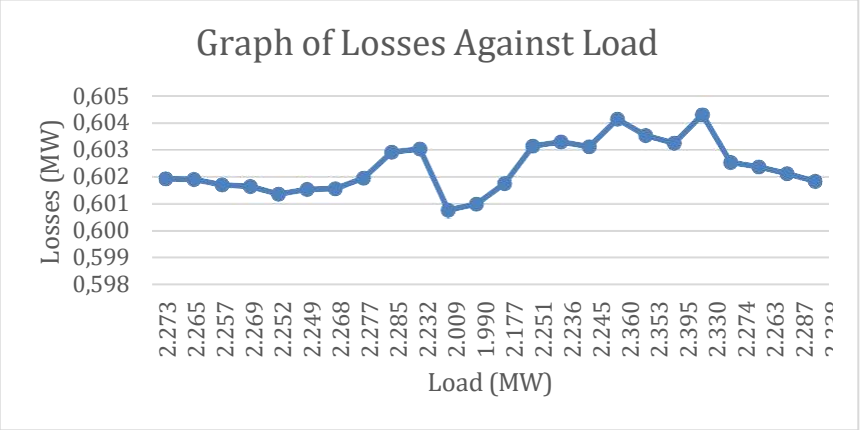

Figure 4. Graph of Losses Against Load 18 May 2024

In Figure 4, the graph of the calculation results for May 18, shows that generator power losses change every hour. The value of these power losses is influenced by the value of the phase current (A) and field current (If) due to changes in load and from the loss graph. The highest power was 0.604 MW at a load of 2.330 MW while the lowest power loss was 0.601 MW at a load of 2.009 MW.

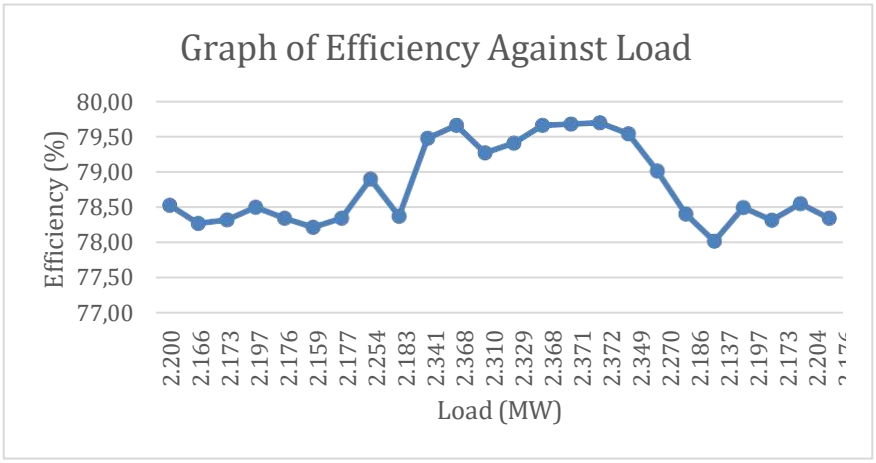

Figure 5. Graph of Efficiency Against Load 17 May 2024

In Figure 5, graph of generator efficiency against load from calculations on May 17, it can be seen that the highest efficiency was 79.69% at a load of 2,372 MW, while the lowest efficiency was 78.03% at a load of 2,137 MW. Changes in the generator power value can affect the generator efficiency value and the generator efficiency value is directly proportional to the generator output power. The greater the generator power value, the greater the efficiency, while the smaller the generator output power value, the smaller the efficiency.

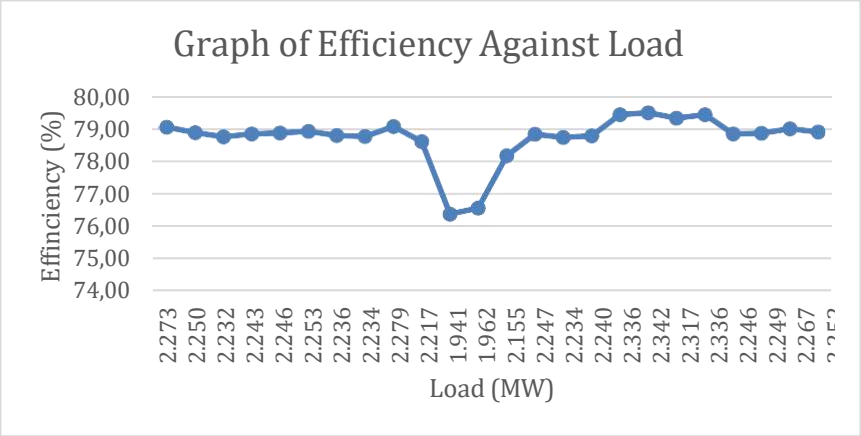

Figure 6. Graph of Efficiency Against Load 18 May 2024

In Figure 6, graph of generator efficiency against load, it can be seen that the highest efficiency was 79.51% at a load of 2,342 MW, while the lowest efficiency was 76.37% at a load of 1,941 MW. The load changes that occur are caused by the generator output power or load being adjusted to the load requirements in the field in order to reduce excess power in the generator output power (Pout) and optimize fuel use which has an impact on the generator efficiency value. With a large generator output power value (Pout), the efficiency value also gets better.

4. Conclusion

Based on the results of research on the effect of changes on the performance of generator unit two of PT. Nusa Daya PLTU Malinau Unit, the following conclusions are obtained:

1. Changes in the generator output power are adjusted to the load requirements in the field which tend to fluctuate and affect the value of the per-phase current as well as the field current or generator excitation.
2. The large values of per-phase current and generator field current cause power losses which are inversely proportional to the generator efficiency value.
3. Based on data from calculation results on May 17, the highest efficiency was 79.69% at a load of 2,372 MW while the lowest efficiency was 78.03% at a load of 2,137 MW and for calculation results on May 18 the highest efficiency was 79.51% at a load of 2,342 MW whereas the lowest efficiency was 76.37% at a load of 1,941 MW.
4. Based on the results of data calculations for 2 days, the average efficiency value on May 17 was 78.81% andon May 18 it was 78.73%.

Reference

[1] E. N. Wijayanti, "ANALISIS PERUBAHAN BEBAN TERHADAP KINERJA GENERATOR PADA PT. PEMBANGKIT JAWA BALI (PJB) – UNIT PEMBANGKIT GRESIK Disusun," *Fish. Res.*, vol. 140, no. 1, p. 6, 2021, [Online]. Available: http://dspace.ucuenca.edu.ec/bitstream/123456789/35612/1/Trabajo de Titulacion.pdf%0Ahttps://educacion.gob.ec/wp-content/uploads/downloads/2019/01/GUIA-METODOLOGICA-EF.pdf%0Ahttp://dx.doi.org/10.1016/j.fishres.2013.04.005%0Ahttps://doi.org/10.1038/s41598-020-

[2] I. Refaldi, Y. Basir, and D. U. Yusa Wardhani, "Analisis Fluktuasi Beban Terhadap Efisiensi Generator Sinkron di PT. PEMBANGKIT LISTRIK PALEMBANG JAYA," *J. Ampere*, vol. 6, no. 2, p. 91, 2022, doi: 10.31851/ampere.v6i2.7293.

[3] M. Muharrir and I. Hajar, "Analisis Pengaruh Beban Terhadap Efisiensi Generator Unit 2 PLTP PT. Indonesia Power UPJP Kamojang," *Kilat*, vol. 8, no. 2, pp. 93–102, 2019, doi: 10.33322/kilat.v8i2.643.

[4] R. SEPTIYAN, M. Waruni K, and B. Sugeng, "Analisa Hilang Daya Pada Generator Sinkron 3 Fasa (6,6 KV) 11 MVA TYPE 1DT4038-3EE02-Z," *J. Tek. Elektro Uniba (JTE UNIBA)*, vol. 4, no. 1, pp. 7–11, 2019, doi: 10.36277/jteuniba.v4i1.45.

[5] Z. Muna, Syahputra, Fauzan, and Julianto, "Studi Perubahan Beban Terhadap Tugi-Rugi Daya Outpur Generator Sinkron Tiga Phase 20 MW Pada Generator Turbin Gas Unit 2 Pada PT Pupuk Iskandar Muda," *J. Tektro*, vol. 7, no. 1, pp. 112–117, 2023.

Biographies of Authors

Andri is an Electrical Engineering Student at the University of Borneo Tarakan in 2019. The author was born in Harapan Maju on January 28 2002. Before becoming a student, the author had completed his education at SMA Negeri 8 Malinau.

Ismit Mado graduated from the ITS Surabaya Doctoral Program in 2019. Currently he serves as Head of the Power System Stability Laboratory at the Department of Electrical Engineering, University of Borneo, Tarakan. He is interested in stability and control studies of power generation systems, forecasting studies based on time series models, and fuzzy modeling.

Muhammad Arif with a Bachelor's degree in Electrical Engineering from Hasanuddin University in 2007. Since 2021 he has been accepted as an employee of PT. PLN Nusa Daya and currently serves as Manager of the customer service unit of PT. PLN Nusa Daya.

Ferry K. Maring graduated from the vocational diploma program from the Indonesian Kristen University in 2012. Worked since 2018 at PT PLN Nusa Daya Unit PLTU Malinau serving as ASMAN OPHAR (assistant manager for operations and maintenance).

Vol. 03, No. 2, December 2024, pp. 93-102
p-ISSN: 2963-8577
e-ISSN: 2964-3511
DOI: 10.57102/jescee.v3i2.92

DESIGN AND IMPLEMENTATION OF A FORWARD-REVERSE DOUBLE-SPEED THREE-PHASE INDUCTION MOTOR CONTROL SYSTEM BASED ON A PROGRAMMABLE LOGIC CONTROLLER

Abdul Muis Prasetia[1*], Linda Sartika[1], Danny Arans Sevri Andika[1]
Electrical Engineering Study Program, Faculty of Engineering, Borneo Tarakan University, Tarakan, Kalimantan Utara

Abstract
The Dahlander motor is an asynchronous AC motor that operates at two or more distinct rotational speeds, making it different from standard three-phase motors, which generally maintain a single speed under the same power conditions. This motor features a squirrel-cage rotor design and is integrated with a programmable logic controller (PLC), which simplifies wiring systems and allows operational adjustments without altering the wiring layout. However, an additional component, the selector switch, is also employed. This switch controls the motor's rotational direction, enabling it to rotate either clockwise or counterclockwise. The study utilizes a quantitative approach with a developmental design to assess the performance of the Dahlander motor control system. The system functioned as expected, with the selector switch responsible for changing rotational direction. In the right position, pressing the ON 1 button activates contactor 1 for slow clockwise rotation, while pressing ON 2 activates contactors 2 and 3 for fast clockwise rotation. In the left position, pressing ON 1 activates contactor 4 for slow counterclockwise rotation, and pressing ON 2 activates contactors 5 and 6 for fast counterclockwise rotation. The measured rotational speeds were as follows: during slow clockwise rotation, the rotor reached 1494 rpm, while for fast clockwise rotation, it hit 3055 rpm. During slow counterclockwise rotation, the rotor speed was 1456 rpm, and for fast counterclockwise rotation, it reached 3050 rpm.

Keywords:
Dahlander motor; PLC; Motor control; Forward reverse

Article History:
Received: November 28th, 2024
Revised: December 11th, 2024
Accepted: December 12th, 2024
Published: December 13rd, 2024

Corresponding Author:
Abdul Muis Prasetia
Electrical Engineering Study Program, Faculty of Engineering, Borneo Tarakan University
Email: prasetia.electric@borneo.ac.id

1. Introduction

The industrial sector in this country has experienced rapid growth, both in large-scale and small-scale sectors. To support efficiency in terms of time and cost, appropriate production equipment is necessary. A significant portion of industrial equipment operates using electric power, particularly induction motors, which are favored for their simple construction, affordability, light weight, efficiency, and ease of maintenance compared to DC motors [1].

The Dahlander motor, also known as a pole-changing or two-speed motor, is a type of multi-speed induction motor where speed is adjusted by altering the number of poles. This is achieved by changing the electrical connections within the motor. Depending on the stator windings, the motor may exhibit either constant or variable torque.

Pole switching in the motor reduces its speed. Robert Dahlander, a Swedish engineer who worked for ASEA, along with his colleague Karl Arvid Lindström, was granted a patent in 1897 for the electrical design that enables pole switching in motors. The Dahlander connection became associated with this new wiring method, and motors

utilizing this configuration are commonly referred to as pole-changing motors or three-phase Dahlander induction motors.

In the industrial sector, three-phase motors are widely used to support operations, particularly in large-scale industries. A commonly employed system is the forward-reverse mechanism. Three-phase induction motors are preferred for their numerous advantages, including simple construction, relatively low cost, and high efficiency. These motors require an alternating current (AC) power supply to operate. The forward-reverse system is widely applied in various industries, such as conveyors, elevators, cranes, and more. In particular, this system is suitable for industries requiring clockwise and counterclockwise rotational operations, such as conveyor applications [2].

Motor control can also be achieved using contactors with the star-delta method, which requires additional components such as a timer to regulate the motor connection transitions. This method minimizes current surges, although the downside is that the installation system becomes complex, requiring extensive wiring to construct the control circuit. Due to the large number of cables needed for control circuit design, this complexity can be reduced by utilizing Programmable Logic Controller (PLC) technology. PLC offers advantages in motor control systems, simplifying operations and reducing the time required for designing or troubleshooting the control system.

2. Method

This study focuses on the design of a Dahlander motor control system using a Programmable Logic Controller (PLC). Proper steps are required in conducting this research to achieve its objectives. These steps follow the flowchart shown in Figure 1, starting with a literature review, which involves examining various sources and theories relevant to this research. The next step involves designing the PLC-based forward-reverse control system for the Dahlander motor. After completing the design, the following stage is creating the ladder diagram using the CX-Programmer software. This step is crucial for operating and executing the Dahlander motor control system via PLC. After the system design is completed, the system configuration process is carried out. This involves verifying whether the equipment used functions according to the instructions and checking the PLC ladder diagram using CX-Programmer. Once this step is complete, the process proceeds to data collection and analysis of the test results.

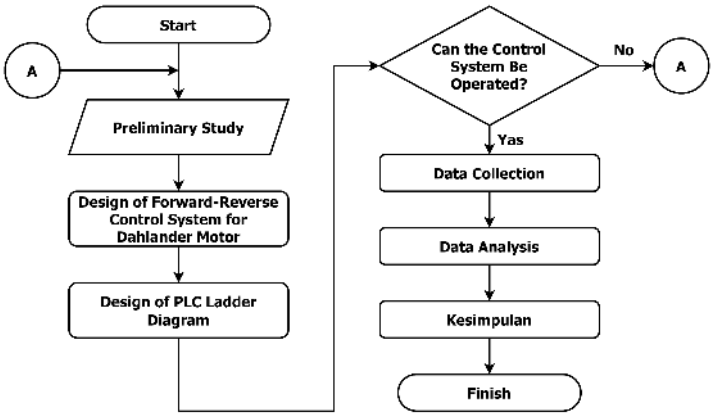

Figure 1. Flowchart of design Dahlander motor control system using PLC

A. Dahlander Motor

The Dahlander motor is a motor with two or more rotational speeds. The presence of two separate windings results in a significantly larger size for three-phase motors designed for two speeds compared to three-phase motors with a single speed at the same power rating. In the Dahlander motor, high speed is achieved using a star (Y) connection, which produces fewer poles, resulting in higher motor speed. For low speed, the motor uses a delta (Δ) connection, which generates more poles, thus leading to slower rotation [6-9]. Each coil in a Dahlander motor has two ends, or in some cases, a center tap for each winding. By altering the connection at the center tap or the

ends of the coil, the number of poles changes, allowing speed adjustment due to the variation in the motor's pole ratio.

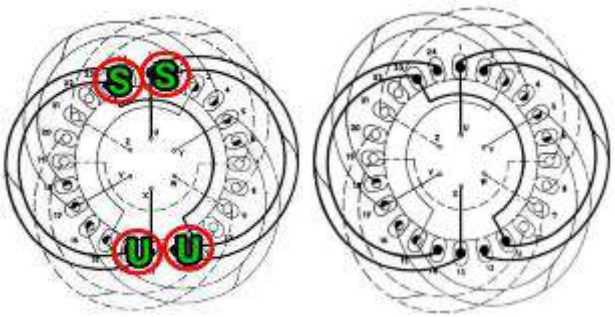

Figure 2. Winding Scheme for 2 Poles

Figure 2 shows a configuration with two poles. The number of poles can be determined using the right-hand rule, where the direction of the current indicates the north pole. In Figure 1, the current starts at slot 1 and moves to slot 11. Slots 1 and 2 form a south pole, while slots 11 and 12 form a north pole. The current then moves from slot 11 to slot 24, continuing to slot 13, where slots 23 and 24 form a south pole, and slots 13 and 14 form a north pole. Figure 2 illustrates that the north poles are located at slots 11, 12, 13, and 14, while the south poles are located at slots 1, 2, 23, and 24. From this, it can be concluded that Figure 2 represents a two-pole configuration.

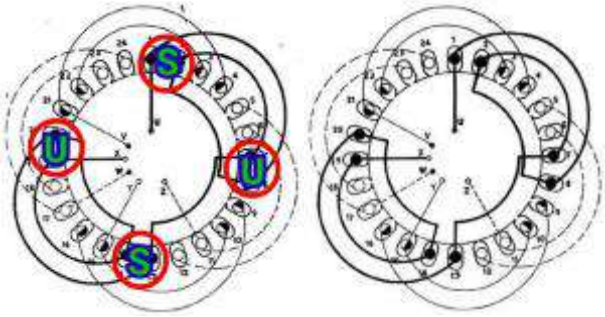

Figure 3. Winding Scheme for 4 Poles

Figure 3 depicts a four-pole configuration. The number of poles is again determined using the right-hand rule. In Figure 3, the winding starts at slot 1 and ends at slot 7. Slots 1 and 2 form a south pole, while slots 7 and 8 form a north pole. The winding then moves from slot 7 to slot 13, ending at slot 19, where slots 13 and 14 form a south pole, and slots 19 and 20 form a north pole. This configuration results in the formation of four poles within the winding.

The equations for calculating the stator rotating field, slip, and rotor speed of the Dahlander motor are presented in Equations (1), (2), and (3), where n_s is the stator speed (rpm), f is the frequency (Hz), p is the number of poles, s is the slip, dan n_r is the rotor speed (rpm):

$$n_s = \frac{120 \times f}{p} \tag{1}$$

$$s = \frac{n_s \times n_r}{n_s} \times 100\% \tag{2}$$

$$n_r = n_s \times (1 - s) \tag{3}$$

B. Programmable Logic Controller

A Programmable Logic Controller (PLC) is a digital electronic device with programmable memory used to store instructions that execute specific functions such as logic, sequencing, timing, counting, and arithmetic operations to control machinery as desired [3]. As its name suggests, PLC incorporates three main concepts: programmable, logic, and controller, which together are used to manage machines or processes.

The operation of a PLC is fundamentally similar to other control devices. It begins with the activation of field devices connected to both the input and output components, which in turn are linked to the machine or other components. During this process, three key scanning phases occur reading and receiving data/signals, executing the programming stored in memory, and updating the state of field devices through the output interface. Once these processes are complete, an interface system is created, enabling the field devices to interact with the controller. The input receives signals, typically instructions from the field devices, while the output executes those instructions accordingly [12-15].

C. Miniature Circuit Breaker (MCB)

An MCB (Miniature Circuit Breaker) is an electrical component that functions to interrupt the flow of electricity when overloading or a short circuit occurs. This interruption serves as a safety measure to prevent undesirable outcomes such as fires. The function of an MCB is similar to that of a fuse, acting as a protective device.

The operating principle of an MCB in normal conditions is as a manual switch, capable of connecting (ON) or disconnecting (OFF) the electrical current. In cases of overload or a short circuit, the MCB automatically interrupts the flow of electricity. This operation can be visually observed as the knob or switch moves from the ON to the OFF position. According to the PUIL 2011, the MCB rating can be determined using Equation (4).

$$Ratting\ MCB\ =\ 250\ \%\times I_n \tag{4}$$

D. Contactor

A contactor is an electronic device used to facilitate the operation of electrical installations or equipment. The contactor operates based on the principle of electromagnetic induction, where an energized coil creates a magnetic field that closes the normally open (NO) contacts and opens the normally closed (NC) contacts [11].

A magnetic contactor is an electromechanical switch capable of connecting and disconnecting a circuit, controlled remotely. The movement of the contacts is driven by electromagnetic force. Magnetic contactors function as switches that rely on magnetism meaning they only operate when magnetism is present. The magnet pulls or releases the contacts. Normal operating current refers to the current that flows when no switching is occurring. The coil of a magnetic contactor is designed specifically for either direct current (DC) or alternating current (AC) [4] and [10]. The formulas used to calculate power and current in a contactor are presented in Equations (5) and (6), where P is power (watt), V is voltage (volt), and $cos\varphi$ is the power factor.

$$P\ =\ \sqrt{3}\times V\times I\times Cos\ \varphi \tag{5}$$

$$I\ =\ \frac{P}{\sqrt{3}\times V\times I\times Cos\ \varphi} \tag{6}$$

E. Hardware Design

This stage begins with preparing the tools and materials for the forward-reverse control system of the Dahlander motor. The next step is determining the layout of the components within the Dahlander motor control panel. The

wiring system is designed and connected to the components in the control panel. Additionally, a full inspection of the completed control system is conducted. The forward-reverse control circuit for the Dahlander motor is shown in Figure 4.

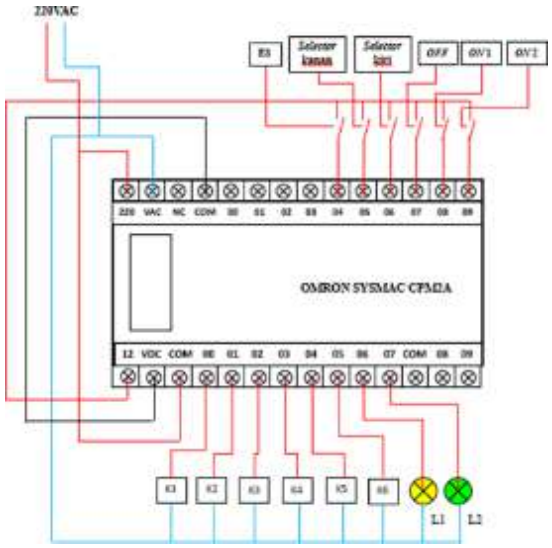

Figure 4. Forward-reverse control circuit for Dahlander motor

C. Software Design

The software design uses a ladder diagram, implemented using the CX-Programmer application. The input and output usage in the PLC system is presented in Table 1.

Table 1. Input and Output Usage on PLC

Component Name	Port	Function
Emergency Stop Button (T. ES)	0.04	Emergency stop button
OFF Button (T. OFF)	0.07	Button to turn off the control system
ON 1 Button (T. ON 1)	0.08	Button to activate slow rotation in both directions
ON 2 Button (T. ON 2)	0.09	Button to activate fast rotation in both directions
Right Selector Switch	0.05	Button to set motor rotation to the right
Left Selector Switch	0.06	Button to set motor rotation to the left
Contactor 1 (K1)	10.00	Output K1 for right-side slow rotation
Contactor 2 (K2)	10.01	Output K2 for right-side fast rotation
Contactor 3 (K3)	10.02	Output K3 for right-side fast rotation
Contactor 4 (K4)	10.03	Output K4 for left-side slow rotation
Contactor 5 (K5)	10.04	Output K5 for left-side fast rotation
Contactor 6 (K6)	10.05	Output K6 for left-side fast rotation
Slow Speed Indicator (L1)	10.06	Indicator light for slow rotation
Fast Speed Indicator (L2)	10.07	Indicator light for fast rotation

C. CX-Programmer

CX-Programmer is a transition software for Omron brand PLCs. To program the PLC, the computer with CX-Programmer must be connected to the PLC processor using a serial cable. Once connected, the PLC parameters

must be configured. There are two ways to configure the controller: Auto Online and Manual. The Auto Online method automatically configures the controller by reading the parameters from it. However, if the controller has already been programmed, using Auto Online may produce an error if the controller's module layout differs from the previous setup. In such cases, manual configuration is required. Manual configuration involves creating a new project, selecting the appropriate controller type (Device Type), and entering the module type used by selecting it [5].

3. Result and Discussion

Based on the design and implementation of the forward-reverse control system for a three-phase induction motor with double speed, controlled by a programmable logic controller (PLC), the specifications of the control panel used for the Dahlander motor are shown in Table 2.

Table 2. Specifications of the Dahlander Motor Control Panel

Specifications	Value
Length	60 cm
Width	40 cm
Depth	20 cm
Voltage	380 VAC
Current	1,38,1,18 A
Power	0,8 kW
Frequency	50 Hz

A. Control Panel Design for Dahlander Motor

The control panel design for the Dahlander motor discusses selecting the appropriate tools and components required for the system.

1. Selecting the Miniature Circuit Breaker (MCB)

The MCB specification must be suitable for the load, in this case, a 3-phase Dahlander motor with a running current of 1.38 A at low speed and 1.18 A at high speed (for clockwise rotation). The MCB rating is calculated using Equation (4), and the result is shown in Table 3. The chosen MCB has a safety limit of 4 Amps based on the obtained results.

$$\begin{aligned} Ratting\ MCB &= 250\ \% \times I_n \\ &= 250\ \% \times 1{,}38 \\ &= 3{,}45\ A \end{aligned}$$

Table 3. MCB Rating Calculation Results for Motor Rotation

Kondisi	Current (A)
Right-side slow speed	3.45
Right-side fast speed	2.95
Left-side slow speed	3.42
Left-side fast speed	2.85

2. Selecting the Contactor

Based on the nameplate, the contactor's current, power, and voltage match the design specifications. During slow clockwise rotation, Contactor 1 operates. During fast clockwise rotation, Contactors 2 and 3 operate. For slow counterclockwise rotation, Contactor 4 works, and for fast counterclockwise rotation, Contactors 5 and 6 are engaged. Power and current in the contactor are calculated using Equations (5) and (6). From the calculations, it is concluded that the minimum contactor capacity required is 2 Amps.

$$P = \sqrt{3} \times V \times I \times Cos\ \varphi$$

$$= \sqrt{3} \times 405{,}1 \times 1{,}1 \times 0{,}92$$

$$= 890{,}819\ Watt$$

$$I = \frac{P}{\sqrt{3} \times V \times I \times Cos\ \varphi}$$

$$= \frac{P}{\sqrt{3} \times 405.1 \times 1{,}1 \times 0{,}92}$$

$$= 1{,}38\ A$$

B. Input and Output System Testing

This phase tests the entire system after design completion. Table 4 presents the test results. When the right selector button is activated, the motor is set to rotate clockwise, but it hasn't started yet. Pressing ON 1 initiates the slow clockwise rotation, indicated by Contactor 1 and a yellow indicator light for slow speed. Pressing ON 2 initiates fast clockwise rotation, signified by Contactors 2 and 3 and a green indicator light for fast speed.

In the forward-reverse control system, when the system is set to clockwise rotation, the counterclockwise system cannot operate. To rotate counterclockwise, press the left selector button, followed by ON 1, which starts the slow counterclockwise rotation, indicated by Contactor 4 and the yellow indicator. Pressing ON 2 initiates fast counterclockwise rotation, indicated by Contactors 5 and 6 and the green indicator. To turn off the system, press the OFF button. In case of an emergency, pressing the emergency stop (ES) button shuts down the entire system.

Table 4. Input and Output Testing Results

Address	***Device***	**Function**	**Note**
0.04	Emergency Stop Button	Shuts down the control system in an emergency	Active
0.05	Right Selector Button	Directs motor rotation to the right	Active
0.06	Left Selector Button	Directs motor rotation to the left	Active
0.07	OFF Button	Turns off the control system	Active
0.08	ON 1 Button (Right & Left, Slow)	Activates slow rotation control for both directions	Active
0.09	ON 2 Button (Right & Left, Fast)	Activates fast rotation control for both directions	Active
10.00	Contactor 1	Controls right-side slow rotation	Active
10.01	Contactor 2	Controls right-side fast rotation	Active

10.02	Contactor 3	Controls right-side fast rotation	Active
10.03	Contactor 4	Controls left-side slow rotation	Active
10.04	Contactor 5	Controls left-side fast rotation	Active
10.05	Contactor 6	Controls left-side fast rotation	Active
10.06	Slow Indicator Light	Indicates slow rotation	Active
10.07	Fast Indicator Light	Indicates fast rotation	Active

C. Testing the Dahlander Motor Control Panel

The purpose of testing the Dahlander motor control panel is to verify that the control system operates correctly. During testing, pressing the right selector button and ON 1 engages Contactor 1, corresponding to a delta (Δ) connection for slow speed. Pressing ON 2 switches to fast speed, activating Contactors 2 and 3, which have a star (Y) connection. Similarly, pressing the left selector button initiates counterclockwise rotation. Contactor 4 is engaged for slow speed with a delta connection, and Contactors 5 and 6 work for fast speed with a star connection. Table 5 displays the test results for both clockwise and counterclockwise rotations.

Table 5. Testing Results of the Dahlander Motor Control Panel for Right and Left Rotation Directions

Input	***Output***	**Status**
Right Selector Button, ON 1 (Slow)	Contactor 1	Active
	Contactor 2	Inactive
	Contactor 3	Inactive
	Contactor 4	Inactive
	Contactor 5	Inactive
	Contactor 6	Inactive
	Slow Indicator Light	Active
	Fast Indicator Light	Inactive
Right Selector Button, ON 2 (Fast)	Contactor 1	Inactive
	Contactor 2	Active
	Contactor 3	Active
	Contactor 4	Inactive
	Contactor 5	Inactive
	Contactor 6	Inactive
	Slow Indicator Light	Inactive
	Fast Indicator Light	Active
Left Selector Button, ON 1 (Slow)	Contactor 1	Inactive
	Contactor 2	Inactive
	Contactor 3	Inactive
	Contactor 4	Active
	Contactor 5	Inactive
	Contactor 6	Inactive
	Slow Indicator Light	Active
	Fast Indicator Light	Inactive
Left Selector Button, ON 2 (Fast)	Contactor 1	Inactive
	Contactor 2	Inactive
	Contactor 3	Inactive
	Contactor 4	Inactive
	Contactor 5	Active
	Contactor 6	Active
	Slow Indicator Light	Inactive

Input	*Output*	Status
	Fast Indicator Light	Active

C. Comparison of Forward-Reverse Circuits Using PLC and Manual Systems

The comparison between PLC-based and manual forward-reverse circuits is based on two variables: installation and timer. The results are presented in Table 6.

Table 6. Comparison Between PLC and Manual Circuits

Variable	PLC	Manual
Circuit Installation	Easier to diagnose issues in case of input or output errors. The cause of malfunction can be identified by simply reading the ladder diagram program.	Difficult to identify malfunctions. If input or output errors occur, manual inspection is required.
Timer	Incorporated in the ladder diagram, functioning as a safeguard during speed changes of the Dahlander motor.	Operates through switches or relays based on preset time intervals, with the timer represented as a physical component in the circuit.

4. Conclusion

From the design and implementation of the 3-phase double-speed induction motor control system using a PLC, it can be concluded that the Dahlander motor control system functions as intended. During the slow clockwise rotation, the nominal current is 1.33 A, and during fast clockwise rotation, it is 1.12 A. For counterclockwise rotation, the current is 1.12 A at slow speed and 1.08 A at fast speed. The manual forward-reverse circuit has a simpler installation compared to the PLC-based system, as the latter requires input-output systems to operate the circuit. However, in practical use, the PLC-based system is superior because it simplifies the operation process, and in case of issues, the PLC is easier to troubleshoot without needing to check the wiring installation. In a manual circuit, a wiring diagram is the primary reference, whereas in the PLC system, a ladder diagram is required to operate the forward-reverse control. The PLC-based system also simplifies troubleshooting since it does not require checking the entire wiring, unlike the manual system.

References

[1] N. Evalina, A. Azis, and Z. Zulfikar, "Pengaturan Kecepatan Putaran Motor Induksi 3 Fasa Menggunakan Programmable Logic Controller," *JET (Journal of Electrical Technology*, vol. 3, no. 2, pp. 73-80, 2018.
[2] Nurfauziah, "Penggunaan rangkaian forward-reverse sebagai pengontrol motor 3 fasa," in *Vocational Education National Seminar (VENS)*, vol. 1, no. 1, 2022.
[3] Capiel, "Programmable logic controller," *artikel ilmiah academia.edu*, 1982.
[4] Prasetyo, *Trainer Pengendali Motor Listrik Ac 3 Fasa*, pp. 8-12, 2016.
[5] R. Yudha, "Perancangan dan Simulasi Trainer Human Machine Interface (HMI) untuk Media Pembelajaran Berbasis CX Designer PLC," *Jurnal Material dan Proses Manufaktur*, 2020.
[6] A. M. Prasetia and H. Santoso, "Implementation of Scalar Control Method for 3 Phase Induction Motor Speed Control," *Elinvo (Electronics, Informatics, and Vocational Education)*, vol. 3, no. 1, pp. 63-69, 2018.
[7] F. Ghoroghchian, A. D. Aliabad, and E. Amiri, "Dual-pole LSPM motor with dahlander winding for high inertia loads," in *2019 IEEE 28th International Symposium on Industrial Electronics (ISIE)*, pp. 308-312, June 2019.

[8] T. Đuran, S. Tvorić, and V. Šimović, "Comparison of Efficiency Level for Induction Motor with Dahlander Winding in Direct on Line and via Frequency Converter Drive Connection," in *2022 45th Jubilee International Convention on Information, Communication and Electronic Technology (MIPRO)*, pp. 142-146, May 2022.
[9] C. Contà and N. Bianchi, "Pole-Changing in Synchronous Machines: A Reluctance-Permanent Magnet Hybrid Motor," *IEEE Transactions on Industry Applications*, 2023.
[10] S. R. Khabibi, J. E. Poetro, and A. T. Nugraha, "Rancang Bangun Panel Sistem Kontrol dan Monitoring Motor 3 Fasa Dual Speed Berbasis Mikrokontroler," *Elektriese: Jurnal Sains dan Teknologi Elektro*, vol. 10, no. 2, pp. 61-68, 2020.
[11] D. Smugala, "Analysis of Dynamic Parameters of the Switching-On Process of Electromagnetic Relays Powered by Harmonic Polluted Voltage Source," *Energies*, vol. 17, no. 12, p. 2872, 2024.
[12] W. Bolton, *Programmable Logic Controllers*, Newnes, 2015.
[13] C. T. Jones, *Programmable Logic Controllers: The Complete Guide to the Technology*, Brilliant-Training, 1998.
[14] D. Ahuja and N. Chaudhary, "Programmable Logic Controller," *International Journal of Information and Computer Science*, vol. 1, pp. 115-120, 2012.
[15] M. Pathade and G. Yeole, "Programmable Logic Controllers (PLC) and its Programming," *International Journal of Engineering Research and Technology*, vol. 3, no. 1, 2014..

Biographies of Authors

Abdul Muis Prasetia is an Assistant Professor of Electrical Engineering, Faculty of Engineering, University of Borneo Tarakan, Tarakan, Kalimantan Utara

Linda Sartika is an Assistant Professor of Electrical Engineering Study Program, Faculty of Engineering, Borneo Tarakan University, Tarakan, Kalimantan Utara

Danny Arans Sevri Andika is an undergraduate final year student at the Department of Electrical Engineering, Universitas Borneo Tarakan, Tarakan, Indonesia.

Vol. 03, No. 2, December 20xx, pp. 103-109
p-ISSN: 2963-8577
e-ISSN: 2964-3511
DOI: 10.57102/jescee.v3i2.93

RISK ASSESSMENT ANALYSIS OF PRESURE VESSEL REFRIGERANT ACCUMULATOR AT PT XYZ

Khusnun Widiyati[1*], Valeska Harianja[1], Hadi Sutanto[2] , Marselinus Bachtiar[3]
[1]Department of Mechanical Engineering, Faculty of Industrial Engineering, Universitas Pertamina
[2]Department of Mechanical Engineering, Universitas Katolik Indonesia Atma Jaya
[3]Department of Industrial Engineering, Universitas Katolik Indonesia Atma Jaya

Abstract
The Refrigerant Accumulator equipment is a pressure vessel located within the production system unit, namely the Dew Point Control (DPC) Unit. The Refrigerant Accumulator is a crucial component within the DPC Unit as it serves as a reservoir for the Propane refrigerant liquid. In case of a failure of this equipment, it would halt the entire process in the DPC Unit and impact the control of gas dew point that is transmitted to consumers through pipelines. Hence, a more effective method is required to prevent failures in the Refrigerant Accumulator. One of the methods that can assist in more effective inspection is Risk-Based Inspection (RBI). Risk-Based Inspection is a risk-based inspection methodology, where the main output obtained is an inspection plan determined based on the risk of the equipment. It prioritizes inspections for equipment with higher risk of damage, thus optimizing equipment maintenance and aiding companies in establishing effective maintenance strategies. Therefore, this study aims to analyze the risk level of the Refrigerant Accumulator equipment using the Risk-Based Inspection method according to API 581, determine the risk level of the Refrigerant Accumulator equipment, and provide appropriate inspection planning recommendations for the Refrigerant Accumulator equipment. Based on the results of this study, the Risk-Based Inspection analysis yielded values for Probability of Failure (PoF), Area-based Consequence (CA), and Financial Consequence (FC) through quantitative calculations based on the steps outlined in API 581. The PoF value is 5.011×10-6, the CA value is 3,316.36 ft2, and the FC value is $22,746,756.91. From the analysis results, the risk level of the Refrigerant Accumulator equipment is categorized as Medium-Risk, with a Probability of Failure of 5.011×10-6 in category 1 and a Consequence of Failure of $22,746,756.91 in category E. Consequently, the final category is 1E, with a remaining life of 33.7 years. Based on the obtained risk level, the recommended inspection planning is to conduct the next inspection on December 2031, using Visual Inspection method with 100% surface coverage and Phased Array Ultrasonic Testing (PAUT) with 90% surface coverage.

Keywords:
Refrigerant accumulator; presure vessel; risk based inspection; probability of failure; consequence of failure

Article History:
Received: December 2nd, 2024
Revised: December 11th, 2024
Accepted: December 12th, 2024
Published: December 13rd, 2024

Corresponding Author:
Khusnun Widiyati
Department of Mechanical Engineering, Universitas Pertamina, Indonesia
Email:
khusnun.widiyati@universitaspertamina.ac.id

1. Introduction

The oil and gas industry are one of the largest economic sectors in Indonesia [1]. The use of oil and natural

gas is crucial for industrial, transportation, and household purposes. The oil and gas industry comprises several stages, including exploration, production, and distribution. Oil and gas companies employ highly complex and diverse equipment such as pressure vessels, relief devices, piping, boilers, heaters, and other production facilities [2,3].

PT. XYZ is a company involved in the oil and gas industry, including exploration, exploitation, and the sale of oil and gas production. PT. XYZ operates numerous central processing plants (CPPs) for gas production, one of which is CPP Matindok located in Central Sulawesi. In the production of gas for delivery to consumers, various equipment and production system units are involved, including the Dew Point Control Unit (DPCU). The DPCU's role is to prevent gas from condensing during transportation through pipelines to consumers [4]. One of the equipment components within the DPCU is the pressure vessel refrigerant accumulator. This pressure vessel serves as a container for refrigerant from the thermosyphon tank, which is then directed to the refrigerant compressor suction drum to cool the gas in the oil separator.

The construction of the pressure vessel refrigerant accumulator began in 2015 and has been in up to date. The refrigerant accumulator is a crucial component in the DPCU, as it serves as a reservoir for refrigerant, which significantly affects the gas dew point control process. Over time, the pressure vessel can experience performance degradation or damage, primarily due to intensive use and environmental conditions. Any failure in the pressure vessel can disrupt or even halt the gas cooling process, potentially leading to accidents or serious incidents, including leaks, fires, and explosions that can endanger personnel, the environment, and company assets. Therefore, it is essential to ensure that the Refrigerant Accumulator is in good and safe working condition. One way to ensure equipment condition is through periodic inspections (time-based) [5]. Periodic inspections are scheduled at fixed intervals, regardless of the actual equipment condition or risk. However, conducting periodic inspections on pressure vessels can consume unnecessary maintenance time, costs, and significant resources.

Based on the preceding paragraph, there is a need for a more effective method to prevent failures in the pressure vessel, not solely based on time but also on equipment risk (risk-based). One method that can help oil and gas companies conduct inspections more effectively is Risk-Based Inspection (RBI). Risk-Based Inspection is a risk-based inspection methodology, where the main output is an inspection plan determined based on the equipment's risk level [2]. Risk-Based Inspection prioritizes inspections on equipment with a higher risk of failure [6], maximizing maintenance on critical equipment and helping oil and gas companies establish sound maintenance strategies.

In this research, a quantitative approach is employed, following the API Recommended Practice 581 2016 Addendum II 2020. API 581 is chosen as the standard code because it is closely related to Risk-Based Inspection and provides detailed quantitative methodology for risk assessment and determining appropriate inspection and maintenance strategies. A quantitative approach is used in this study due to its higher precision compared to qualitative methods. By applying a quantitative approach, detailed calculations can be obtained, and we can determine the appropriate inspection planning and mitigation methods for the pressure vessel refrigerant accumulator.

Based on the background outlined. The main objectives of this study are as follows: (1) conducting a risk analysis of the Refrigerant Accumulator using the Risk-Based Inspection method in API 581; (2) determining the risk level of the Refrigerant Accumulator; and (3) proposing recommendations for an appropriate inspection plan for the Refrigerant Accumulator.

2. Method

This risk assessment is conducted based on Risk Based Inspection (RBI) methodology as stated in American Petroleum Institute (API) 581. API 581 [5] provides a basis for quantifying risk systematically. The philosophy stems from the source of failure, that is the loss of containment from the pressurized boundary resulting in leakage or rupture from the pressurized containment. The output of the assessment if risk ranking which serves as the basis for conducting inspection as well as performing mitigation tasks. Figure 1 shows the methodology of RBI as stated in API 581 [5].

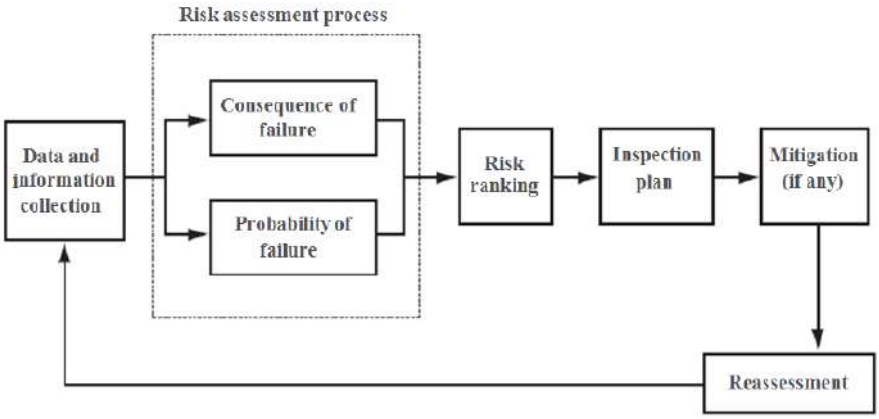

Fig. 1. Risk Assessment Methodology [5]

A. Data Collection

The problem identified in this research is the pressure vessel refrigerant equipment in the Dew Point Control Unit (DPCU), which was built in 2015. The DCPU has only been inspected once in 2021, and no assessment has been conducted on the pressure vessel equipment, therefore, the risk associated with the pressure vessel is unknown. The data required for the risk assessment analysis consists of P&ID and PFD, equipment design data, inspection and equipment history data, process operation data, factor management system data, cost factors (replacement or repair costs, waste mitigation costs, injury costs), and population density.

B. Risk Assessment

The process of performing risk assessment analysis is shown in Figure 1. The risk assessment analysis includes the calculation of Probability of Failure (PoF) and Consequence of Failure (CoF). The relationship between risk, POF and COF is shown in equation (1). The output of the risk assessment is risk ranking. From the risk ranking, inspection plan and mitigation plan can be made accordingly. This cycle is repeated by updating the information from the inspection and mitigation activity.

$$\text{Risk} = \text{Probability of Failure} \times \text{Consequence of Failure} \quad (1)$$

C. Probability of Failure

The Probability of Failure (Pf(t)) is obtained by deriving the generic failure frequency (gff), management system factor (FMS) and damage factor (Df(t)).

$$Pf(t) = gff \cdot Df(t) \cdot FMS \quad (2)$$

Generic failure frequency is a probability of failure developed for specific component type based on a large population of component data that does not include the effect of specific damage mechanism [2]. Management system factor indicates the evaluation of facility's management system, which may consists of plant management, operations, inspection, maintenance, engineering, training and safety personnel. The management system factor may be obtained through a series of interviews. The higher the facility scores indicate the low value of FMS, which eventually contributes to low probability of failure. Damage factor describes the mechanism by which the damage occurs. There are several types of damage mechanism, such as thinning, stress corrosion cracking, high hydrogen attack, mechanical fatigue, etc. API 571 [7] provides identification for several damage factors.

D. Consequence of Failure (CoF)

The consequence of failure (CoF) is analyzed from two categories, namely the consequence area (CA) and

the consequence of financial (CF). The consequence area is determined from the impact when a certain amount of working fluid under observation is to be released. The release type, whether instaneous or continuous also play important roles in determining the amount of fluid released. The impact is observed from the damage area resulted if the working fluid is flammable; and also from the number of population affected if the working fluid contains toxicity. On the other hand, consequence financial is accounted by the cost for replacement or repair component, cost of loss of production, cost of accidents, cost of damage to equipment or component around it and cost of environmental pollution.

E. Case Study

The equipment investigated in this study is a pressure vessel refrigerant accumulator located in DPC Unit, CPP Matindok. The refrigerant accumulator has undergone inspection only once, which was the measurement of wall thickness on December 7, 2021, using the Non-destructive Testing (NDT) method, specifically Ultrasonic Testing. The measurement was performed on several components of the pressure vessel, taking the minimum thickness. The damage mechanism identified to occur in DPC unit are thinning and external corrosion. The value of generic failure frequency is obtained from API 581, which is 0.0000306 failures/year for pressure vessel [5]. The Management System Factor (FMS) is obtained by performing survey. The FMS value has been determined based on the results of an audit conducted at the company and is equal to 0.43.

3. Result and Discussion

In this research, the refrigerant accumulator was divided into several components, namely: shell 1, shell 2, head front, head rear , nozzle 1, nozzle 2 and nozzle 3. The purpose of the division is to understand the risk possesses on each component constructing the refrigerant accumulator. Tabel 2 shows the summary of variabel needed to calculate the probability of failure.

Table 1. Probability of Failure (PoF)

Component	gff	Df(t)	FMS	POF	***Category***
Shell-1	0.0000306	0.3808	**0.43**	**5.01×10^{-6}**	**1**
Shell-2		0.3669		**4.82×10^{-6}**	**1**
Head-front		0.2122		**2.79×10^{-6}**	**1**
Head-rear		0.2147		**2.82×10^{-6}**	**1**
Nozzle-1		0.1466		**1.93×10^{-6}**	**1**
Nozzle-2		0.1609		**2.11×10^{-6}**	**1**
Nozzle-3		0.1667		**2.19×10^{-6}**	**1**

The highest probability of failure for components constructing the refrigerant accumulator is 5.01×10-6, by which this value is classified as category 1, according to API 581 [7].
The fluid contained in the refrigerant accumulator is flammable and is not in the form of steam, acids, or caustics. In addition to that, the fluid does not contain toxicity. The evaluation regarding the area-based flammable consequences calculation for both component damage and personnel injury can be seen in Table 2.

Table 2. Component Damage and Personnel Injury Consequence Area

Component Damage CA	1,305.91 ft2
Personnel Injury CA	3,316.36 ft2

The value of the Final Consequence Area is determined from the highest value between component damage or personnel injury. Therefore, the consequence area is taken from personnel injury consequence are, which is 3,316.36 ft2. Thus number is classified as category C according to API 581 [5]

The calculation of financial consequences is based on the recommendations from API 581, as well as the costs for equipment replacement, production loss, population density, and personnel injury costs. The financial

consequence for this case is estimated to be $22,746,756.91. This number is categorized as E class, according to API 581 [5].

Based on the analysis of the Probability of Failure (PoF) and Consequence of Failure (CoF), these values are input into the risk matrix. The risk ranking for the pressure vessel refrigerant accumulator equipment in term of areas based is shown in Figure 2. From this figure, it can be observed that the risk for area based in classified as low risk.

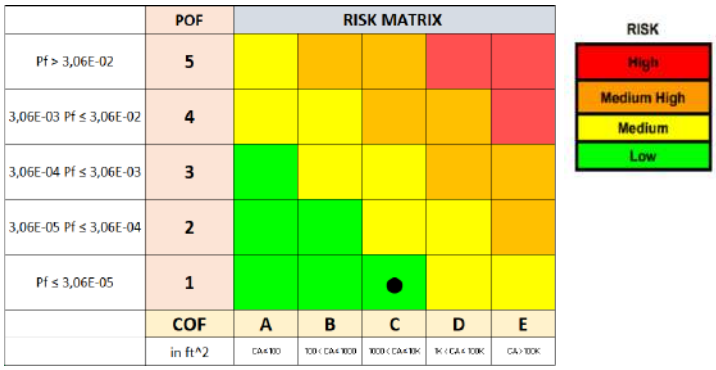

Figure 2 Area-based Risk Matrix

In addition to that, another risk matrix is constructed to determine the risk ranking in term of financial based. Figure 3 shows the risk ranking for financial based. From this figure it can be observed that the financial risk is categorized as medium risk.

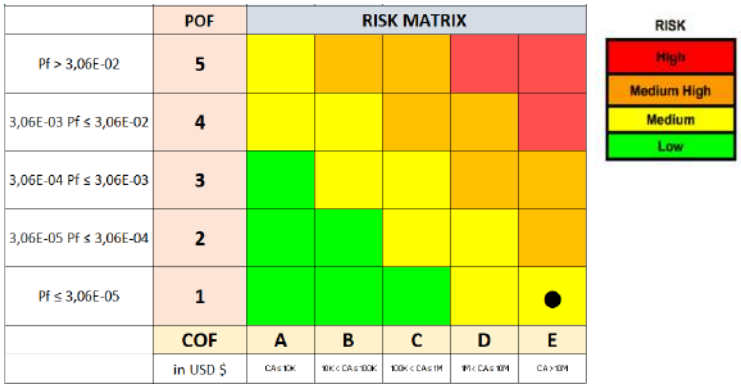

Figure 3 Financial-based Risk Matrix

From the two risk ranking shown in Fig. 2 and Fig. 3, the inspection plan and mitigation plan can be formulated by taking consideration of the highest possible risk posses by the refrigerant accumulator. Therefore, the risk level for the refrigerant accumulator equipment is category 1E (Medium-risk).

The remaining life of the refrigerant accumulator can be calculated to be 33.7 years with corrosion rate to be 0.186 mm/year. Since the remaining life of the equipment is greater than 10 years, therefore, according to API 510 [8] the next inspection date can be determined as 10 years from the previous inspection date. As stated previously that the previous inspection date was performed on December 2021, therefore, the next inspection date is expected to be performed on December 2031. The inspection plan to be performed can be formulated based on API 572 Section 9 [10], by which, the inspection method for the internal thinning damage factor is to perform Non-destructive Examination (NDE). The selected NDE method is based on the guidelines in ASME Sec. V Non mandatory Appendix E – Computerized Imaging Techniques [11], specifically the Phased Array Ultrasonic Testing (PAUT) method.

For external corrosion, according to API 572 Section 9 [10] the recommended method for the External Corrosion damage factor is visual inspection of the entire surface and components of the pressure vessel. This inspection should include checking for damaged areas, cracks, bolt tightness, the condition of paint coatings, supports, handrails, and corrosion indications.

4. Conclusion

Based on the results of the conducted research, the conclusion of the research is:

1. Risk analysis was performed using the Risk-based Inspection method by calculating the Probability of Failure (PoF) and Area-based Consequence (CA), as well as Financial Consequence (FC), based on API 581. The probability of failure is 5.011×10-6, the consequence of failure is 3,316.36 ft2, and the financial consequence is expected to be $22,746,756.91.
2. The risk level of the Pressure Vessel Refrigerant Accumulator is in the Medium-Risk category, with a Probability of Failure of 5.011×10-6 in category 1 and a Consequence of Failure of $22,746,756.91 in category E. The remaining life of the refrigerant accumulator is expected to be 33.7 years.
3. The proposed inspection planning is to conduct the next inspection in 10 years from the last inspection, which is on December 7, 2031, using the visual inspection method with 100% surface coverage, and using the Phased Array Ultrasonic Testing (PAUT) method with 90% surface coverage.

References

[1] Kementerian Koordinator Bidang Perekonomian, "Menjadi Penopang Pertumbuhan Ekonomi, Menko Airlangga Dorong Industri Migas Tingkatkan Penggunaan Produk Dalam Negeri," 28 Juli 2022. [Online]. Available: https://ekon.go.id/publikasi/detail/4392/menjadi-penopang-pertumbuhan-ekonomimenko-airlangga-dorong-industri-migas-tingkatkan-penggunaan-produk-dalamnegeri.
[2] American Petroleum Institute API 580, Risk-based Inspection API RECOMMENDED PRACTICE 580, Washington, DC: American Petroleum Institute, 2016.
[3] M. S. Isdiawan, "Perbandingan Performa Refrigeran Propana dan Amonia pada," JURNAL REKAYASA PROSES, vol. 15, no. Jurnal UGM, pp. 94-115, 2021.
[4] S. K. Rosmiani Ahmad, "An overview of time-based and condition-based maintenance," Computers & Industrial Engineering, pp. 135-149, 2012.
[5] American Petrolium Institute API 581, Risk-Based Inspection Methodology API RECOMMENDED PRACTICE 581, Washington, DC: American Petroleum Institute, 2016.
[6] G. Prasetyo, "Penilaian Risiko dan Perencanaan Inspeksi pada Sistem Perpipaan Menggunakan Metode Risk Based Inspection," Institut Teknologi Sepuluh Nopember, Surabaya, 2018.
[7] American Petroleum Institute API 571, Damage Mechanisms Affecting Fixed, America Petroleum Institute, 2011.
[8] American Petroleum Institute API 510, Pressure Vessel Inspection Code, American Petroleum Institute, 2006.
[9] MENTERI ENERGI DAN SUMBER DAYA MINERAL, PERATURAN MENTERI ENERGI DAN SUMBER DAYA MINERAL REPUBLIK INDONESIA NO. 18 TAHUN 2018, MENTERI ENERGI DAN SUMBER DAYA MINERAL, 2018.
[10] American Petroleum Institute API 572, Inspection Practices for Pressure Vessels RP 572 4th Edition, American Petroleum Institute, 2016.
[11] ASME Section V, ASME Boiler & Pressure Vessel Code Nondestructive Examination, New York: The American Society of Mechanical Engineer, 2019.

Biographies of Authors

Khusnun Widiyati
Lecturer at the Department of Mechanical Engineering, Universitas Pertamina. Her reasearch interest includes maintenance and reliability, risk based inspection, and product design.

Valeska Harianja Author 2 short CV and photograph
Student at the Department of Mechanical Engineering, Universitas Pertamina.

Vol. 03, No. 2, December 2024, pp. 111-119
p-ISSN: 2963-8577
e-ISSN: 2964-3511
DOI: 10.57102/jescee.v3i2.94

ELECTRICAL NETWORK PROTECTION SYSTEM ON THE CILEGON-CIBINONG CONDUCTOR USING A DEFENSE SCHEME WITH OVER GENERATION SHEDDING (OGS) AT PT PLN (PERSERO) UIP2B JAMALI

Devi Febiola Pardede
Department of Electrical Engineering, Faculty of Industrial Technology, Universitas Pertamina

Abstract
A Defense Scheme is a protection mechanism designed to normalize the frequency by reducing load or generation. It serves as a safeguard for electrical facilities, access control for system management, routine maintenance to ensure the security and reliability of power system operations, and even as a pre-planned crisis management tool to address emergencies and disturbances in the electrical system. Several types of defense schemes are employed to address or prevent overload shedding (OLS) and Oover generation shedding (OGS). With the rapid advancements in technology, particularly in the industrial sector, innovative solutions have become increasingly sophisticated. One example is the maintenance system for power plants, which can be optimized through the creation of an operational plan (RENOP) aimed at enhancing efficiency and performance. This includes analyzing the design of electrical network protection systems using the Defense Scheme for over generation shedding (OGS).

Keywords:
Force measurement; uncertainty; weighted least squares (WLS); biomimetics; robotics

Article History:
Received: November 11th, 2024
Revised: December 11th, 2024
Accepted: December 12th, 2024
Published: December 13rd, 2024

Corresponding Author:
Devi Febiola Pardede
Department of Electrical Engineering, Universitas Pertamina, Indonesia
Email: devifebiolaa@gmail.com

1. Introduction

With the rapid advancements in future technologies, the role of higher education institutions in Indonesia becomes increasingly significant. The Electrical Engineering Study Program at Universitas Pertamina plays a critical role in contributing to technological progress by equipping students with both theoretical knowledge and practical skills. These competencies are fundamental for students as they prepare for the demands of the professional world. To this end, the program emphasizes the importance of practical training, where students gain real-world work experience, reinforce their skills and knowledge in areas relevant to their field of study, expand professional networks, and prepare themselves to enter the workforce after graduation.

The current technological advancements, particularly in the industrial sector, have reached unprecedented levels of sophistication. As one of the key players in the energy industry, PT PLN (Persero) Unit Induk Pusat Pengatur Beban Jawa, Madura, Bali (UIP2B JAMALI) is pivotal in the operation and maintenance of power plants and load control systems. These systems are essential for supporting industrial activities and ensuring the reliability of energy supply. One of the strategic approaches to optimizing the maintenance and performance of power plants is through the development of an Operational Plan (RENOP). This plan aims to enhance efficiency and performance by analyzing the design of electrical network protection systems, specifically employing the Defense Scheme Over Generation Shedding (OGS).

A Defense Scheme is a protection mechanism activated during abnormal operating conditions in the power system that can lead to frequency deviations. This scheme is designed to restore frequency stability by either reducing load or generation. It serves multiple functions, including safeguarding electrical facilities, controlling system access, ensuring operational security through routine maintenance, and implementing pre-planned crisis management to handle emergencies and disturbances in the power system.

Defense Schemes are tailored to the specific topology and conditions of the power system. Two notable types are Overload Shedding (OLS) and Over Generation Shedding (OGS). OLS is utilized to alleviate excessive load conditions, while OGS addresses scenarios where generation surpasses demand. By employing these schemes, power system operators can ensure the stability and reliability of the grid, which is essential for the smooth operation of modern industries.

In the context of the industrial revolution and the growing reliance on renewable energy, the application of Defense Schemes is increasingly critical. Research has shown that adopting advanced defense mechanisms significantly enhances grid resilience and minimizes the risk of outages during abnormal conditions. For instance, a study by Chen et al. (2023) highlights the effectiveness of OGS in managing renewable energy intermittency. Similarly, Smith et al. (2022) emphasize the role of RENOP in improving power plant efficiency and reliability. These findings underscore the importance of integrating advanced protection schemes, such as OGS, into the operation and maintenance of power systems.

Through practical training opportunities at institutions like PT PLN (Persero) UIP2B JAMALI, students at Universitas Pertamina are exposed to real-world challenges and solutions in the field of electrical engineering. This experience not only enhances their technical skills but also prepares them to contribute meaningfully to the development and implementation of cutting-edge technologies in the energy sector.

2. Method

A. Planning and Implementation of the Defense Scheme

The steps involved in the planning and implementation of the Defense Scheme are as follows:

a. Proposal and Review of Defense Scheme Scenarios
The operational system function proposes new Defense Scheme scenarios or reviews existing scenarios due to changes in system parameters, the addition of new installations, or unanticipated disturbances that are not covered by the existing Defense Scheme.

b. Coordination with UP2B
The operational system function at the central unit coordinates with UP2B to conduct a study of the Defense Scheme. The output of this process is a recommendation for the Defense Scheme scenario.

c. Discussion and Consensus Building
Discussions are held with the operational system function, transmission, distribution, generation, regional, and project functions regarding the recommended Defense Scheme scenario. The output is a meeting record containing the agreed-upon Defense Scheme scenario for implementation.

d. Engineering Design
The operational system function designs the engineering aspects of system protection equipment for the Defense Scheme in coordination with the installation owners (transmission/distribution/generation). The output is an approval drawing document from the installation owner.

e. Protection System Coordination
Settings and coordination of system protection equipment are discussed among the operational system function and installation owners.

f. Installation and Commissioning
The operational system function installs and commissions the Defense Scheme with assistance from the installation owner.

g. Documentation and Reporting
The operational system function issues a report on the installation and commissioning of the Defense Scheme scenario, signed by both the operational system function and the installation owner. The implemented Defense Scheme is documented in a Defense Scheme manual.

B. Evaluation of Defense Scheme Performance

The steps for evaluating the Defense Scheme performance are as follows:

a. Detection of System Disturbances
The operational system function detects system disturbances that activate the Defense Scheme.

b. Performance Records and Reports
The operational system function at the central unit and UP2B records the Defense Scheme performance during disturbances. UP2B submits disturbance and performance reports to the central unit.

c. Performance Evaluation

The central unit evaluates the Defense Scheme performance to ensure 100% effectiveness. If the Defense Scheme operates successfully, an assessment is conducted to verify alignment with targets or load quota realization.

d. Investigation of Malfunctions
If the Defense Scheme does not achieve 100% effectiveness, the operational system function and the installation owner jointly investigate malfunctioning equipment.

e. Recommissioning
Post-investigation, the malfunctioning Defense Scheme equipment undergoes recommissioning and reevaluation to ensure performance.

f. Final Reporting
The operational system function issues a recommissioning report for the Defense Scheme scenario, signed by the operational system function and the installation owner.

C. Over Generation Shedding (OGS)

Over Generation Shedding (OGS) is a generation-limiting scheme implemented through relays to manage or secure current flow into equipment, ensuring it does not exceed line protection limits by tripping generators or opening circuit breakers (PMTs). Power systems often face unavoidable disturbances, such as sudden trips on feeders due to overloading or natural disruptions causing conductor breaks. The input for OGS activation is typically the current [7]. OGS aims to reduce power flow in overloaded transmission lines, inter-bus transformers (IBTs), or transformers by tripping generators. It is a type of Defense Scheme designed to prevent overloads or blackouts in electrical systems. In recent studies, OGS has proven effective in mitigating the risks of overloads and blackouts in power systems. According to Chen et al. (2023), implementing advanced Defense Schemes like OGS enhances grid stability and reduces operational risks. Furthermore, Smith et al. (2022) emphasized the importance of coordination among operational functions to ensure the effective deployment of OGS in modern power systems. The integration of OGS also aligns with the increasing complexity of renewable energy systems. For example, Zhang et al. (2021) demonstrated that OGS significantly improves the reliability of transmission networks under high renewable penetration. These findings underscore the importance of adopting systematic approaches to Defense Scheme planning and evaluation.

3. Result and Discussion

A. Power System

In general, an electrical power system consists of three main components: power generation, power transmission, and power distribution. A modern power system is a complex network comprising power generation plants, transmission lines, and distribution networks. These components work together to deliver electricity from generation centers to load centers [1]. To achieve the operational objectives of an electrical power system, the generation, transmission, and distribution components must function as an integrated unit, as illustrated in Figure 2 below.

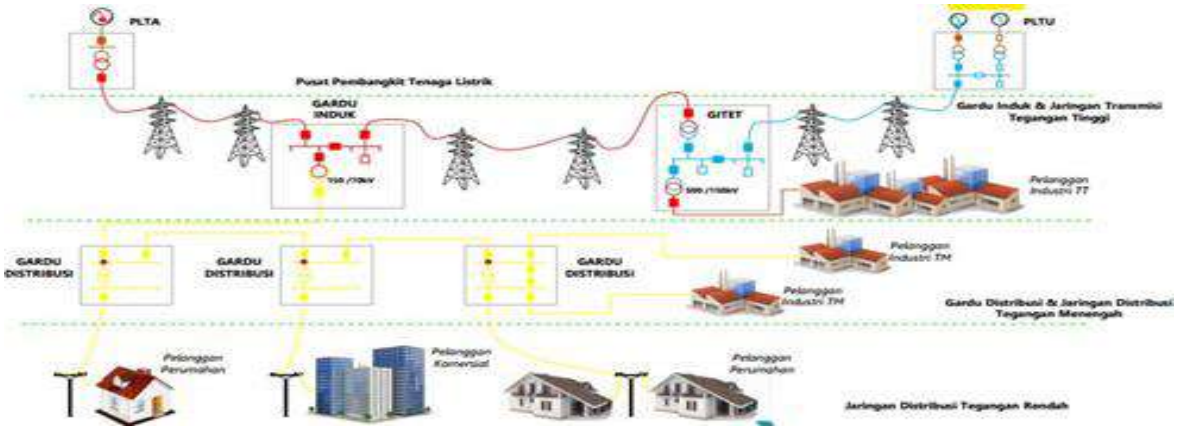

Figure 1. Power System Grid

Electrical power systems are critical for ensuring the reliable and efficient delivery of electricity to meet societal demands. The three primary components are interconnected and must work seamlessly to achieve optimal performance:

a. Power Generation
The generation component is responsible for producing electricity. This is typically achieved using various energy sources, such as fossil fuels, nuclear energy, or renewable resources like wind, solar, and hydropower. Power plants are strategically located based on resource availability, economic considerations, and proximity to major load centers.

b. Power Transmission
Transmission systems transport electricity over long distances from power generation plants to substations near load centers. This is achieved using high-voltage transmission lines to minimize power losses. Transmission networks often include interconnected systems that enhance reliability and enable efficient energy exchange between regions.

c. Power Distribution
The distribution system delivers electricity from substations to end users. This component involves medium- and low-voltage networks designed to meet the specific requirements of residential, commercial, and industrial customers. Distribution systems often employ smart technologies to enhance monitoring, control, and reliability.

B. Modern Power System Challenges

Modern electrical power systems face several challenges due to increasing demand, the integration of renewable energy sources, and the complexity of maintaining stability and reliability. Some of these challenges include:

1. **Renewable Energy Integration**: The variability of renewable energy sources such as wind and solar requires advanced grid management techniques to ensure consistent power delivery [2].
2. **Grid Stability**: Maintaining frequency and voltage stability is critical, especially with the increasing use of distributed energy resources (DERs) [3].
3. **Aging Infrastructure**: Many power systems operate with aging equipment, which necessitates upgrades to maintain efficiency and reliability [4].

C. Importance of Integration

The seamless integration of generation, transmission, and distribution is essential for a resilient and sustainable power system. For example, advancements in smart grid technology allow for real-time monitoring and control, enabling better coordination across all components. Additionally, the adoption of advanced protection schemes, such as Defense Schemes discussed earlier, further enhances system reliability by mitigating risks associated with overloads and faults.

To achieve the objectives of electrical power system operations, three main aspects must be considered: economics, reliability, and quality. However, the prioritization of these aspects can vary depending on real-time conditins. In the event of disturbances, security becomes the primary priority, while quality and economic factors take a backseat. When security and quality are stable (normal conditions), economic considerations should take precedence. This dynamic prioritization ensures the effective and reliable operation of the power system under varying circumstances.

D. Key Operational Conditions

The operation of a power system involves different states, which are categorized as follows:

1. Normal Condition
- All consumers are served without interruptions.
- Operational constraints are resolved.
- System security requirements are met.

2. Alert Condition (Siaga)
- All consumers are still served without interruptions.
- Operational constraints are managed, but system security is compromised.
- This condition may indicate the system is at risk, requiring immediate attention to avoid further degradation.

3. Emergency Condition

- Some or all consumers cannot be served due to system failures.
- Operational constraints are not met, leading to a potential risk of blackouts or cascading failures.
- Emergency actions, such as load shedding or isolating faulted sections, are necessary to prevent total system collapse.

4. **Recovery Condition**
   - This is a transitional phase from an emergency state back to normal operation.
   - Voltage and frequency are closely monitored and maintained within specified ranges to ensure stability during recovery.
   - The operational conditions of a power system are illustrated in Figure 3, which visually represents the transitions and priorities during these states.

E. Real-Time Prioritization and Challenges

The prioritization of objectives in a power system highlights the complexity of real-time operation and control. These priorities must adapt to changing conditions to maintain system stability and service continuity. Below is a detailed explanation of how each priority functions under specific conditions:

1. **Economics**
   - Economic operation involves optimizing generation and transmission costs while maintaining efficiency.
   - Under normal conditions, operational strategies prioritize minimizing production costs and transmission losses, often using economic dispatch and unit commitment methods.
2. **Reliability**
   - Reliability ensures uninterrupted power supply to consumers.
   - This includes planning for contingencies, maintaining redundancy in transmission paths, and ensuring rapid response to faults or disturbances.
3. **Quality**
   - Power quality pertains to maintaining voltage and frequency within acceptable ranges.
   - Poor power quality can result in equipment damage, reduced efficiency, or consumer dissatisfaction.

F. Practical Considerations in Operational Conditions

a. **In Normal Conditions**
   Economic optimization tools, such as optimal power flow (OPF), are employed to achieve cost-effective operation while maintaining quality and reliability.
b. **In Alert Conditions**
   Operators must identify risks and take preventive measures, such as reconfiguring the network or redistributing loads, to prevent escalation into an emergency.
c. **In Emergency Conditions**
   Immediate corrective actions, including load shedding or activating Defense Schemes (e.g., Over Generation Shedding), are required to stabilize the system and prevent widespread outages.
d. **In Recovery Conditions**
   Coordination among generations, transmission, and distribution is critical to restoring normal operation. System operators may prioritize reconnecting critical loads and gradually restoring service to other areas.
e. **Importance of System Security**
   System security is a cornerstone of power system operation, especially during disturbances. It involves real-time monitoring, dynamic reconfiguration, and deploying protection mechanisms to mitigate risks. Advanced tools, such as supervisory control and data acquisition (SCADA) systems, enable operators to respond quickly and maintain stability.

G. OGS Scheme on the Cilegon-Cibinong Transmission Line Using DigSilent

The Cilegon-Cibinong Transmission Line is a high-voltage transmission network project connecting Cilegon in Banten with Cibinong in West Java, Indonesia. This project aims to enhance the reliability of electricity supply and strengthen interconnections between electrical systems across Java. Spanning approximately 130 kilometers and operating at 500 kV, this transmission line is a critical component of the region's power infrastructure [3]. Over Generation Shedding (OGS) is an automated regulation system in power networks used to prevent overvoltage and overfrequency conditions caused by excess power generation that surpasses system demand. For high-voltage transmission lines like the Cilegon-Cibinong line, implementing an OGS scheme ensures the stability

of the power system under varying operational conditions. The OGS scheme for the Cilegon-Cibinong transmission line can be analyzed using DigSilent, a powerful simulation tool for power system analysis. By incorporating the system's parameters and the OGS scheme into the simulation, DigSilent enables the evaluation of OGS performance under various operating conditions. The main objectives of the DigSilent simulation are to assess the effectiveness of the OGS scheme in mitigating overvoltage and over frequency issues, to evaluate the performance of the power system during peak load conditions and disturbances, to identify potential improvements to the system's reliability and security.

The schematic representation of the Cilegon-Cibinong transmission line in DigSilent is illustrated in Figure 4.

Figure 2. Cilegon – Cibinong Feeder Model

From the schematic representation of the Cilegon-Cibinong Extra High Voltage Transmission Line 1 (SUTET Cilegon-Cibinong 1), the results for daytime peak load (BP) during workdays and the secured equipment are summarized as follows:

a. Key Observations from Table 1: Daytime Peak Load Conditions

1. Peak Load Analysis:
    - The daytime peak load represents the maximum electrical demand on the transmission line during regular workday hours.
    - This analysis identifies the stress on the transmission line under typical operational conditions, particularly during high-demand periods.
2. Secured Equipment:
    - Specific equipment along the transmission line is evaluated for its ability to operate within safe limits under peak load conditions.
    - Protective measures, such as Over Generation Shedding (OGS), are implemented to ensure that critical components are safeguarded against potential overloads or failures.

b. Importance of Peak Load Analysis and Equipment Security

Analyzing peak load conditions is critical for understanding the operational performance of high-voltage transmission lines and ensuring the stability and reliability of the power system. Below are the key points elaborated:

1. Peak Load Conditions:
    - During peak load periods, the transmission line is subjected to its highest capacity utilization, making it essential to evaluate its operational performance.
    - Factors such as increased power demand, temperature effects on conductors, and potential bottlenecks in power flow are assessed to ensure the line can handle these conditions.
2. Secured Equipment:

- Equipment security refers to ensuring that transformers, circuit breakers, protection relays, and other critical components are not exposed to conditions that could lead to failures.
- The OGS scheme plays a vital role in maintaining equipment security by automatically shedding excess generation or diverting loads to prevent overvoltage and overfrequency conditions.

3. Use of Over Generation Shedding (OGS):
   - OGS is particularly significant during peak load conditions as it helps prevent system instability caused by excess generation.
   - By dynamically balancing the power flow, OGS ensures that all equipment operates within its designed specifications, thereby prolonging the lifespan of system components.
4. Impact on System Reliability:
   - Ensuring the security of equipment under peak load conditions minimizes the risk of cascading failures and outages.
   - A well-functioning OGS scheme improves the overall reliability of the transmission system and supports uninterrupted power delivery to consumers.

c. Application of Data in System Planning and Operations

The results of peak load analysis and equipment security measures serve multiple purposes in system planning and operations:

- Operational Planning: Real-time data on peak load conditions inform operational decisions, such as dispatching generation units or rerouting power flows to avoid overloading specific lines.
- Preventive Maintenance: Identifying equipment at risk during peak load conditions allows for targeted maintenance schedules, reducing the likelihood of unplanned outages.
- System Expansion: Insights from peak load studies guide infrastructure expansion projects, such as upgrading transmission capacity or adding redundancy to improve system resilience.

Future Directions

- Dynamic Load Monitoring: Advanced monitoring tools, such as synchrophasors, can provide real-time insights into load variations and equipment performance under dynamic conditions.
- Integration with Smart Grids: Incorporating smart grid technologies, such as demand response and distributed generation, can alleviate peak load stress on transmission lines.
- Enhanced Simulation Studies: Using sophisticated simulation tools like DigSilent, operators can model various peak load scenarios and their impact on system stability and reliability.

Table 1. Daytime Peak Load Condition of SUTET Cilegon-Cibinong 1

Loading and Voltage							
Normal Condition				N-2 Maintenance Trip of the SUTET Depok-Gandul 2 Circuits			
SUTET	MW	%	kA	SUTET	MW	%	kA
DEPOK-CIBNG 1	729	42	0.840	DEPOK - CIBNG 1	26	4	0.063
DEPOK-CIBNG 2	729	42	0.840	DEPOK - CIBNG 2	26	4	0.063
DEPOK-GNDUL 1	702	41	0.809	DEPOK - GNDUL 1	0	0	0
DEPOK-GNDUL 2	702	41	0.809	DEPOK - GNDUL 2	0	0	0
JAWA7-BLRJA 2A	982	45	1.128	JAWA7 - BLRJA 2A	698	32	0.799
JAWA7-BLRJA 1A	982	45	1.128	JAWA7 - BLRJA 1A	698	32	0.799
SRLYA-BLRJA 1	1129	33	1.298	SRLYA - BLRJA 1	707	20	0.816

SRLYA-BLRJA 2	1129	33	1.297	SRLYA - BLRJA 2	707	20	0.815
SRLYA-CLBRU 1	937	55	1.087	SRLYA - CLBRU 1	1649	97	1.938
SRLYA-CLBRU 2	937	55	1.087	SRLYA - CLBRU 2	1649	97	1.938
CLBRU-CIBNG	915	44	1.065	CLBRU-CIBNG	2272	114	2.732
CIBNG-TAMBUN 1	872	51	1.005	CIBNG - TAMBUN 1	843	51	1.004
CIBNG-TAMBUN 2	870	51	1.006	CIBNG - TAMBUN 2	841	51	1.006
Loading and Voltage							
Normal Condition				N-2 Maintenance Trip of the SUTET Depok-Gandul 2 Circuits			
Voltage KV	KV	%	kA	Voltage KV	kV	ΔV	kA
LESTARI BANTEN ENERGI7	505			LESTARI BANTEN ENERGI7	505	0	
SURALAYA BARU7	505			SURALAYA BARU7	505	0	
SURALAYA LAMA7	505			SURALAYA LAMA7	505	0	
NEWBALARAJA7	502			NEWBALARAJA7	505	-3	
CILEGONBARU7	503			CILEGONBARU7	501	2	
JAWA7	505			JAWA7	506	-1	
GORDA	145			GORDA	144	1	
PUNCAK ARDI MULYA	145			PUNCAK ARDI MULYA	144	1	
IBT	KV			IBT	kV		
IBT1_1SRLYA75	117			IBT1_1SRLYA75	117		
IBT2_1SRLYA75	111			IBT2_1SRLYA75	112		
IBT1_1CLBRU75	297			IBT1_1CLBRU75	297		
IBT2_1CLBRU75	297			IBT2_1CLBRU75	297		
IBT3_1CLBRU75	349			IBT3_1CLBRU75	349		
IBT1_1BRAJA75	261			IBT1_1BRAJA75	244		
IBT2_1BRAJA75	261			IBT2_1BRAJA75	244		
IBT3_1BRAJA75	193			IBT3_1BRAJA75	180		
IBT4_1BRAJA75	193			IBT4_1BRAJA75	180		
IBT1_1DEPOK75	74			IBT1_1DEPOK75	91		
IBT2_1DEPOK75	49			IBT2_1DEPOK75	62		
Generators	MW	Mvar		Generators	MW	Mvar	
PLTU SURALAYA 1-8	3752	655		PLTU SURALAYA 1-8	3752	780	
PLTU LBE	625	106		PLTU LBE	625	127	
PLTGU CILEGON	196	59		PLTGU CILEGON	196	59	
PLTU LABUAN	227	68		PLTU LABUAN	227	68	
PLTU LONTAR 1,2,3	726	138		PLTU LONTAR 1,2,3	726	136	
PLTU JAWA 7	1982	337		PLTU JAWA 7	1982	403	
Total PLTU Suralaya 1-8+LBE+Jawa 7	6359			Total PLTU Suralaya 1-8+LBE+Jawa 7	6359		

Based on the peak load and voltage data of the SUTET Cilegon-Cibinong 1 during daytime maintenance conditions, when SUTET Depok-Gandul 2 circuits are tripped, the CLBRU-CIBNG generator experiences an overload in both power and current. In normal conditions, the SUTET Cilegon-Cibinong transmission line delivers a power output of 915 MW with a current level of 1.065 kA. While during the maintenance trip of both Depok-Gandul circuits (N-2) on workdays, the load on the Cilegon-Cibinong transmission line increases significantly. The generated power and current rise to 2,272 MW and 2.732 kA, respectively, representing an increase of 114% from the baseline. The generator shifts from operating at 44% of its capacity under normal conditions to handling an additional 114% load, risking thermal stress, reduced efficiency, and potential damage to system components.

4. Conclusion

Over Generation Shedding (OGS) is an automated or manual action (though manual actions are rarely used) to cut the electricity supply from power plants when there is an oversupply in the power system. OGS is typically implemented when the oversupply cannot be managed through other measures, such as increasing electricity demand by adding generation units or enhancing the capacity of the transmission network. OGS is commonly carried out to avoid power outages (total blackout), which can result in significant economic and social losses.

The use of the Defense Scheme Over Generation Shedding (OGS) is one of the options in power system protection that helps prevent system damage that could lead to network disturbances. Additionally, OGS can minimize the impact of damage on the system and accelerate system recovery in the event of a disturbance. However, OGS can also cause inconvenience for customers who experience unexpected power outages due to the sudden interruption of electricity supply.

Acknowledgment

The authors gratefully acknowledge the support and research facilities provided by Universitas Pertamina.

References

[1] file.pdf. Diakses pada 07 Februari 2023. https://lontar.ui.ac.id/file?file=digital/131528T%2027577Studi%20analisis-Tinjauan%20literatur.pdf.
[2] Wisnu Sri Nugroho. Mengenal Sistem Tenaga Listrik [wordpress]. Diakses pada 10 Maret 2023. https://catatanwsn.wordpress.com/2017/11/11/meng enal-sistem-tenaga-listrik/.
[3] PORTAL-PLN. Diakses pada 07 Maret 2023. https://portal.pln.co.id/.
[4] C. W. T. McLyman. Transformer and Inductor Design Handbook. CRC Press. 2017.
[5] E. Hajipour, M. Salehizadeh, M. Vakilian, and M. Sanaye-Pasand. Residual Flux Mitigation of Protective Current Transformers Used in an Autoreclosing Scheme. IEEE Transactions on Power Delivery. vol. 31 no. 4 pp. 1636–1644. Agustus 2016. doi:10.1109/TPWRD.2015.2480773
[6] E. Noviyani. Studi Pelepasan Beban pada Skema Pertahanan (Defence Scheme) Jaringan Sistem Khatulistiwa. Journal:eArticle Universitas Tanjungpura. 2016. Diakses pada 02 Maret 2023. https://www.neliti.com/id/publications/191211/
[7] H. C. Bagus. Analisa Implementasi Relai OGS Sebagai Proteksi Sistem 500KV Suraya- Balaraja dan Suraya-Cilegon Dengan Menggunakan Etap 6-0. Universitas Mercu Buana, 2012. Diakses pada 03 Maret 2023. https://repository.mercubuana.ac.id/20818/

Biographies of Authors

Devi Febiola Pardede graduated in 2024 with a Sarjana Teknik degree from the Department of Electrical Engineering at Universitas Pertamina. He is currently employed as an engineer at a private company in Jakarta.

ISSN 2963-8577

ISSN 2964-3511

Faculty of
Industrial Technology
Universitas Pertamina
Jl. Teuku Nyak Arief, RT.7/RW.8, Simprug, Kec. Kby. Lama, Kota Jakarta Selatan, Daerah Khusus Ibukota Jakarta 12220